



Towards high-fidelity simulations of coastal submesoscale baroclinic instabilities with MPAS-O (vE3SM3.0.0) Part II: Realistic experiments

Dylan R. Schlichting¹, Katherine M. Smith¹, Mark R. Petersen¹, Robert D. Hetland², Kyle E. Hinson², and Darren Engwirda^{1,3}

¹Los Alamos National Laboratory, Los Alamos, NM, USA

²Pacific Northwest National Laboratory, Richland, WA, USA

³Commonwealth Scientific and Industrial Research Organisation, Australia

Correspondence: Dylan R. Schlichting (dschlichting@lanl.gov)

Abstract. River plumes can strongly influence coastal dynamics but are poorly represented in global ocean models due to stringent resolution requirements. Following the idealized simulations presented in a companion paper (Hinson et al., 2026), this study presents submesoscale-permitting realistic simulations using unprecedented regional refinement with MPAS-O. We assess MPAS-O's ability to represent river plume dynamics by comparing with a validated ROMS configuration focused on the Mississippi–Atchafalaya (M-A) plume in the northern Gulf of Mexico (GoM). The variable-resolution mesh spans 1.4 km in the GoM to 100 km in the Pacific and Indian Oceans. We incorporate several improvements to the representation of river forcing in MPAS-O: the pseudo point source treatment of runoff, river temperature prescribed from air temperature, and passive tracers to track freshwater transport. MPAS-O generates vigorous submesoscales in the open GoM, as quantified by probability density functions of surface relative vorticity and divergence. While the model qualitatively captures the M-A plume's seasonal evolution, it does not realistically reproduce the summer submesoscale eddy field on the Texas–Louisiana shelf. A persistent brackish lens associated with reduced vertical mixing forms and is present throughout the M-A plume. We hypothesize that this arises from interacting parameterization and structural design choices within MPAS-O that affect plume stratification and instability growth under realistic forcing, rather than from deficiencies in numerics. Our results demonstrate MPAS-O's potential for simulating submesoscale processes in the open ocean while highlighting challenges in using regional refinement to model coastal dynamics.

1 Introduction

In Hinson et al. (2026) (hereinafter Part I), we evaluated the Model for Prediction Across Scales–Ocean (MPAS-O; Ringler et al. (2013)) in its representation of coastal submesoscale baroclinic instabilities using idealized simulations of the Mississippi–Atchafalaya (M-A) River plume. MPAS-O simulations were compared with those from the Regional Ocean Modeling System (ROMS; Shchepetkin and McWilliams (2005)) across a range of horizontal resolutions to assess the influence of numerical formulation and subgrid-scale parameterizations on submesoscale dynamics—which had not yet been addressed with



MPAS-O. We found that at kilometer-scale resolutions, horizontal resolution exerted a stronger influence on the simulated dynamics than the choice of ocean model, indicating that MPAS-O maintains high numerical fidelity when representing coastal submesoscale processes. Here, we extend our assessment to realistic simulations. Previous studies with other unstructured global models (e.g., FESOM, ICON, SCHISM) have shown promise in their ability to represent coastal processes (Danilov et al., 2017; Mathis et al., 2022; Zhang et al., 2023), but did not focus on submesoscale dynamics.

The study site for this model-model comparison is the Texas–Louisiana (TXLA) shelf. On the inner shelf (inshore of 50 m depth), the seasonal circulation is modulated by regional winds (Zhang et al., 2012a, 2014). On the outer shelf (50-100 m depth), interactions with Loop Current (LC) eddies can play an important role in the circulation (Zhang et al., 2012a, 2014). During summer (JJA), a weakly upcoast diurnal land–sea breeze in near-resonance with the regional inertial period causes freshwater from the Mississippi–Atchafalaya (M–A) rivers to accumulate on the shelf, forming a surface-advected, submesoscale eddy field (DiMarco et al., 2000; Hetland, 2017; Qu et al., 2022). In contrast, during non-summer months, downcoast winds narrow the plume along the shelf and shift it toward a bottom-advected, frictionally influenced state, rendering it too constricted to support eddies with characteristic diameters of 20-50 km (Hetland, 2017; Kobashi and Hetland, 2020; Zhang et al., 2014). Then, the submesoscale activity better resembles “submesoscale soup” – chaotic and largely unorganized fronts and filaments. As a result, the TXLA shelf exhibits a pronounced seasonal transition between submesoscale eddy-rich and eddy-suppressed regimes. This predictable variability makes the TXLA shelf a natural laboratory for testing a global model’s ability to capture the seasonal evolution of coastal submesoscale processes.

We present two submesoscale-permitting, regionally-refined simulations of the Gulf of Mexico (GoM) with MPAS-O that transition to non-mesoscale-eddy for much of the global domain (Fig. 1a–b). The simulations use unprecedented horizontal (1.4 km) and vertical (0.5-1.0 m, Fig. 2) resolutions for MPAS-O in a realistic configuration within the study region. We compare the MPAS-O simulations with a validated ROMS model that has been used to extensively study this region. Earlier iterations of the ROMS model focused on skill assessment and characterization of the larger-scale shelf circulation (Hetland and DiMarco, 2012; Zhang et al., 2012a, 2014), while more recent work has emphasized submesoscale processes (Kobashi and Hetland, 2020; Qu et al., 2022). The model statistically reproduces key characteristics of the eddy field with unbiased errors (Kobashi and Hetland, 2020). In addition, a two-way nested configuration resolves submesoscale frontal dynamics and has demonstrated skill in reproducing observed processes such as inertially modulated slantwise vertical exchange (Qu et al., 2021, 2022; Schlichting et al., 2023). Given this demonstrated capability, the ROMS setup serves as a robust, process-resolving reference for evaluating MPAS-O simulations on the TXLA shelf.

The broader goal of this study is to identify the limits of regional refinement in an unstructured ocean model originally developed for global applications and highlight development needed to seamlessly integrate the representation of submesoscale coastal processes into global models. We first provide a preliminary evaluation of MPAS-O’s representation of submesoscale processes in the open GoM, followed by a detailed assessment on the TXLA shelf, including the model’s ability to represent submesoscales and the larger-scale seasonal circulation of the M-A plume. As we will show, increasing grid resolution alone is not necessarily sufficient for representing coastal processes in global models. Limitations may arise when models apply forcings in ways that are ill-posed for coastal processes, lack appropriate grid-scale and flow-aware parameterizations, or

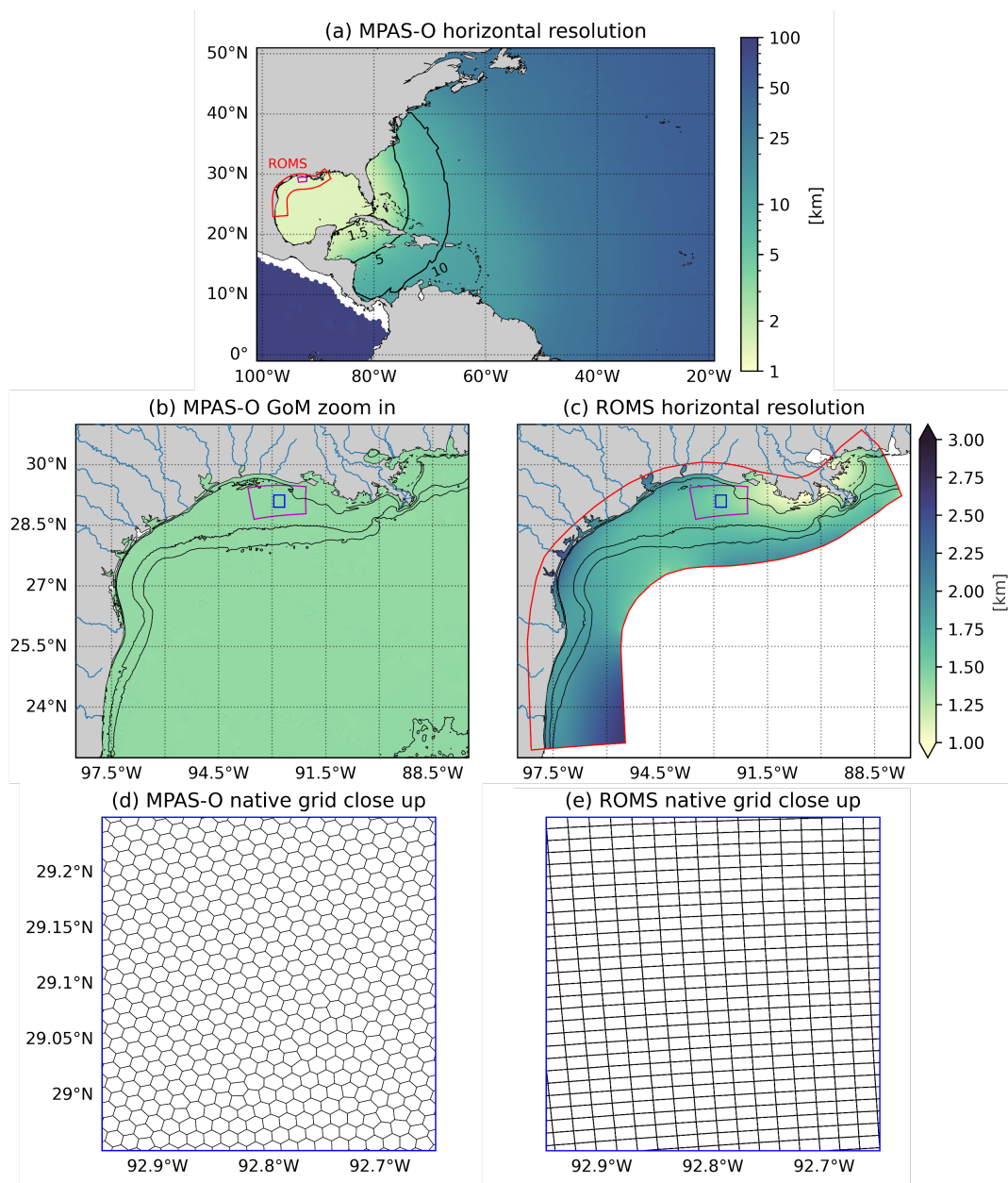


Figure 1. MPAS-O and ROMS horizontal meshes. (a) MPAS-O horizontal resolution, with the 1.5, 5, and 10 km contours marked in black. (b) MPAS-O zoom in the northern Gulf of Mexico, with the 10, 50, and 100 m isobaths marked in black. (c) ROMS model domain and horizontal resolution. The purple box marks the region on the inner shelf used for later statistical analysis. The blue box highlights a close up of the individual cells for (d) MPAS-O and (e) ROMS.

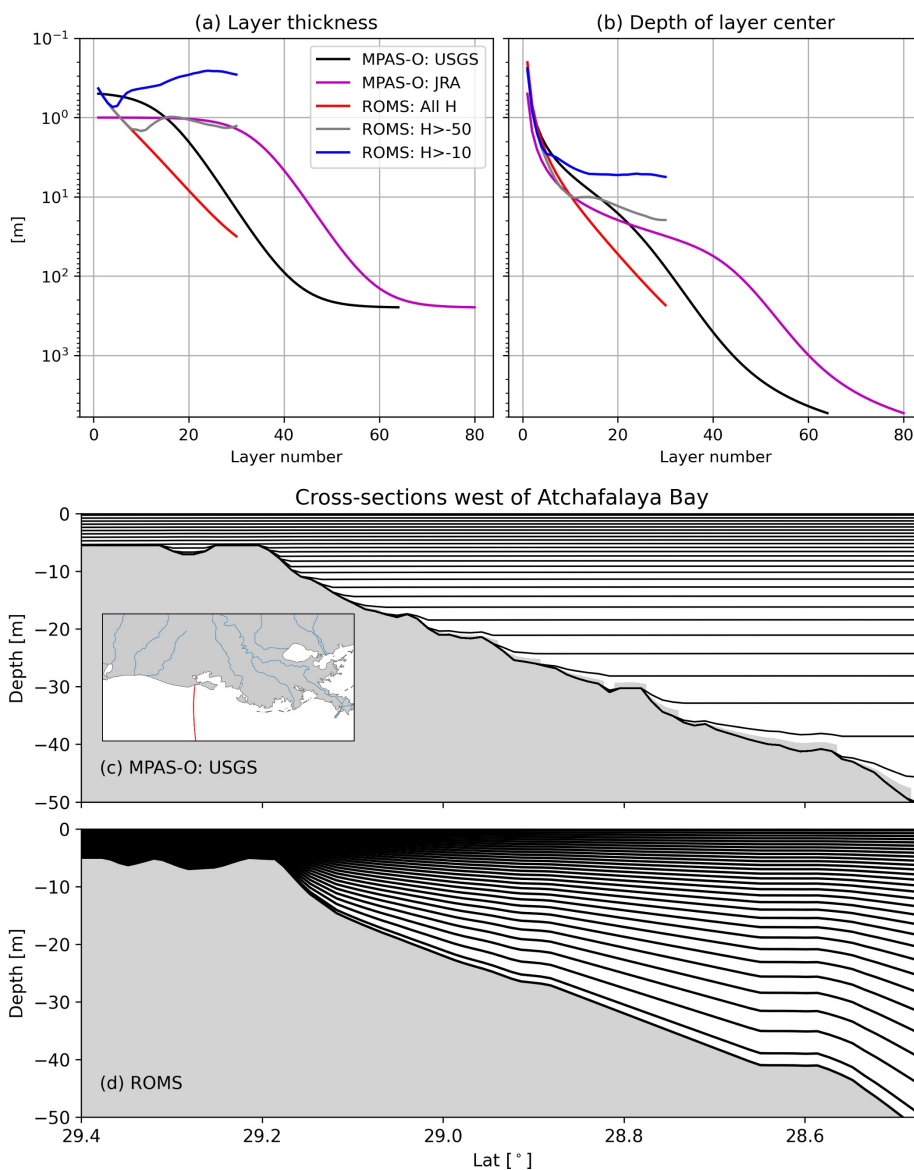


Figure 2. Vertical meshes for MPAS-O and ROMS. (a) Layer thickness, (b) depth of layer center, and sample cross-sections of vertical levels for (c) MPAS-O and (d) ROMS. The red, gray, and blue lines highlight spatial averages of ROMS layer thickness and mid-layer depth for the whole domain, and where the bottom depth H is greater than -50- and -10-m, respectively. The cross-section location is inset in (c).

suffer from numerical errors that become more pronounced as new processes are resolved (Schlichting et al., 2023, 2024). The analyses that follow therefore assess both the dynamical fidelity of the MPAS-O simulations and the practical limitations of regional refinement for representing coastal submesoscale processes in global ocean models.



60 2 Model setup

A detailed description of the MPAS-O and ROMS solution techniques are provided in Part I. The time-stepping, momentum advection, and tracer advection schemes are unchanged from Part I and are summarized in Table 1 for convenience. One key difference in the present simulations is that the online diagnostics used in Part I to quantify physical and numerical tracer mixing following Burchard and Rennau (2008) are disabled. These diagnostics increase computational run time by 50–85%
65 depending on domain decomposition and are not required to achieve the objectives of this study.

2.1 ROMS

ROMS is configured as part of the Coupled-Ocean-Atmosphere-Wave-Sediment Transport Model (COAWST v3.8, Shchep-
etkin and McWilliams, 2005; Warner et al., 2005) implementation. Several versions of this model have been used to study
processes on the TXLA shelf (Kobashi and Hetland, 2020; Schlichting et al., 2023, 2024; Zhang et al., 2014). The domain
70 covers the TXLA shelf and outer continental slopes (Fig. 1c). The curvilinear mesh has 1.28×10^5 horizontal cells with a mean
resolution of 1.7 km; a finer horizontal resolution of 650 m at the M-A River mouths, expanding out to 3.7 km on the outer
continental slopes. The model uses 30 terrain-following vertical layers refined at the surface (Fig. 2). The vertical resolution
ranges from $\mathcal{O}(20$ cm) close to the coast to $\mathcal{O}(100$ m) near the seafloor on the continental slope. Mean vertical resolutions for
the entire domain, inshore of 10 m depth, and inshore of 50 m depth are shown in Fig. 2 (a) to better compare with the MPAS-O
75 simulations. The minimum water depth is 5 m. The model uses a 75 s baroclinic timestep and a 1.5 s barotropic timestep.

The vertical mixing scheme deserves special consideration. To be consistent with the last version of the model used for
validation (Kobashi and Hetland, 2020), we use the $k - \omega$ scheme for our “base case” (hereinafter ROMS: $k - \omega$), which solves
prognostic equations for turbulent kinetic energy k and specific dissipation rate ω . We also perform a simulation using the
ROMS-specific implementation of the K-Profile Parameterization (KPP, hereinafter ROMS: KPP), which is closest to the KPP
80 formulation included in the MPAS-Ocean configuration of the Community Vertical Mixing (CVMix) library (Large et al.,
1994; Van Roekel et al., 2018). See Part I (Hinson et al., 2026) for a more detailed discussion on the differences between
ROMS’ native KPP scheme and the CVMix implementation. Background viscosity and diffusivity values for the simulations
can be found in Table 1. Other aspects of this simulation are the same as ROMS: $k - \omega$. Lateral mixing is parameterized with
harmonic viscosity ($\nu_2^y = 5.0$ m²s⁻¹) and diffusivity coefficients ($\kappa_2 = 1.0$ m²s⁻¹) scaled to the grid size. Lateral viscosity is
85 rotated along terrain-following layers and lateral diffusion is rotated along geopotential surfaces.

The simulations use repeat year forcing (RYF) from 2003-2004 (Stewart et al., 2020). RYF is advantageous because it makes
it easier to identify model differences that could be obscured by interannual variability. A downside is that it prevents us from
validating the simulations with regional climatologies. Because the ROMS model statistically reproduces the characteristics of
submesoscale eddies and captures the seasonal variability of the M-A plume dynamics (Kobashi and Hetland, 2020), we treat
90 this as the reference when comparing to MPAS-O. ROMS uses a virtual salt flux surface boundary condition.

Japanese Reanalysis (JRA) v1.3 is used to provide the following atmospheric forcings every three hours on a 55 km grid
(Stewart et al., 2020): 10 m air temperature, pressure, and winds; specific humidity; downward longwave and shortwave radi-



Table 1. Summary of ROMS and MPAS-O model setup. Differences in intra-model setup are denoted with a comma. In the description of lateral boundary conditions, N, S, E, and W refer to north, south, east, and west, respectively. Note that closed boundaries refer to free-slip conditions for the 2D and 3D velocities, no-gradient conditions for tracers, and no-gradient for the free-surface.

Parameter	ROMS: $k - \omega$, ROMS: KPP	MPAS-O: JRA, MPAS-O: USGS
Horizontal cells	1.3×10^5	1.3×10^6
Horizontal res. [km]	0.6–3.7	1.4–100
Vertical layers	30	80, 64
Vertical res. [m]	0.1–435	1.0–250, 0.5–250
Momentum advection	Third-order upwind (horz) & Fourth-order centered (vert) (Shchepetkin and McWilliams, 1998)	Second-order centered (Ringler et al., 2010)
Tracer advection	MPDATA (Smolarkiewicz and Margolin, 1998)	Flux corrected transport (Skamarock and Gassmann, 2011)
Baroclinic time-stepping	Third-order Adams Bashforth (Shchepetkin and McWilliams, 2009)	Second-order Adams Bashforth (Golaz et al., 2025)
Baroclinic Δt [s]	75	30
Barotropic time-stepping	Leapfrog third-order Adams-Moulton with forward-backward feedback	Second-order forward backward (Higdon, 2005)
Barotropic Δt [s]	1.9	1.5
Tracer time-stepping	Second-order leapfrog with trapezoidal corrector	First-order forward Euler
Vertical mixing	$k - \omega$ & Native KPP	CVMix KPP
Background ν_v [m^2s^{-1}]	$10^{-5}, 10^{-4}$	10^{-4}
Background κ_v [m^2s^{-1}]	$10^{-6}, 10^{-5}$	$10^{-5}, 0$
ν_4^u [m^4s^{-1}]	None	3×10^7 to 1.0×10^{13} , 2.0×10^7 to 8.0×10^{12}
ν_2^u [m^2s^{-1}]	0.9 to 5.0	3.0 to 220, 2 to 110
κ_2 [m^2s^{-1}]	0.2 to 1.0	None
Bottom stress	Quadratic	Quadratic
Bottom drag coefficient	10^{-3}	10^{-3}
Atmospheric forcing	JRA v1.3 RYF	JRA v1.3 RYF
River runoff flux	USGS & USACE	JRA-River, USGS & USACE & JRA-River
River temperature	Stefan and Preud’homme (1993)	JRA 10 m air temperature
2D boundary conditions	All: Closed (N); Free-surface: Chapman-explicit (S,E,W); Momentum: Shchepetkin (S,E,W)	All: Closed (at the coast)
3D boundary conditions	All: Closed (N); Momentum & tracers: Radiation (S,E,W); Turbulent kinetic energy: No-gradient (S,E,W)	All: Closed (at the coast)
Surf. boundary conditions	Virtual salt flux	Kinematic volume flux



95 ation; and precipitation. Outgoing longwave is parameterized using the model sea surface temperature. The model applies a Jerlov water type that transitions from Type III near the river mouths to Type IA near the open boundaries (Jerlov, 1951; Paulson and Simpson, 1977). Outgoing shortwave is parameterized using a constant albedo of 0.06 to be consistent with MPAS-O. Open boundary and climatology forcing is provided by daily output from Global HYCOM Reanalysis, which uses a horizontal resolution of $1/12^\circ$ (see Code and Data Availability). The model is initialized on Jan 1 from the HYCOM climatology file. Tides are neglected in all simulations because they are relatively weak in the GoM (DiMarco and Reid, 1998).

Rivers are configured as point sources (Fig. 3c), using United States Geological Survey (USGS) and United States Army
100 Corps of Engineers (USACE) streamflow data from nine regional rivers (see Code and Data Availability): Mississippi, Atchafalaya, Sabine, Calcaseiu, Trinity, Brazos, San Antonio, Lavaca, and Nueces. The overwhelming majority of the transport comes from the M-A rivers (Zhang et al., 2012b). For each river, the runoff flux, runoff direction, vertical distribution, temperature, and salinity are prescribed. Horizontal momentum associated with river inflows is represented by prescribing volume fluxes along with their vertical distribution across river cell faces; ROMS then computes horizontal velocities and accounts for the resulting
105 momentum through flux divergence. Volume fluxes for the M-A rivers are distributed as piecewise functions to resemble observations, with the majority of the discharge in the upper 13 layers. For the other rivers, volume fluxes linearly decrease over all 30 layers starting from 6.5% in the top vertical layer. The river salinity is set to zero and temperature is prescribed using the approach by Stefan and Preud'homme (1993).

The spinup time is two years, consistent with previous studies (Große et al., 2019; Hetland, 2017), after which the M-A
110 freshwater volume on the shelf remains relatively constant with respect to the day of year. This is quantified by tagging the M-A rivers with passive dyes similar to Zhang et al. (2012a), who used an earlier version of the ROMS model to study freshwater transport on the shelf. This is discussed more in § 3.3. The simulations were run for five years on 120 CPU cores (one node has 128 cores) at the National Energy Research Scientific Computing Center. ROMS: $k - \omega$ achieved approximately 1.9 simulated years per wall-clock day (SYPD), ROMS: KPP achieved 2.1 SYPD. Snapshots and averages of all variables were saved every
115 12 hours. Analysis of model output was done from years three through five.

2.2 MPAS-O

The simulations use the E3SMv3.0.0 version of MPAS-O (Golaz et al., 2025), only differing in the mesh and a few notable
120 additions to rivers and analysis members described below. The model uses a 30 s baroclinic timestep and a 1.5 s barotropic timestep. The unstructured horizontal mesh is generated using the JIGSAW library (Engwirda, 2017). The mesh has 1.26×10^6 horizontal cells consisting of hexagons and pentagons (Fig. 1d). The target resolution in the GoM is 1.5 km to match the mean resolution of the ROMS model on the inner shelf (Fig. 1e), but the actual resolution is 0.95-1.4 km, with the majority of cells falling near the upper range. The target-resolution in the entire GoM is uniform to minimize any potential impacts of flow impedance on LC dynamics. The remainder of the mesh transitions to a target resolution of 60 km in the Atlantic and 100 km in the Pacific and Indian Oceans (not shown) using hyperbolic tangent functions similar to Hoch et al. (2020). Actual resolutions
125 are closer to 55 and 95 km, respectively. The resolution is sub-10 km across part of the North Atlantic and Caribbean Sea (Fig. 1a). We note that high resolution cells in the GoM "leaked" across the Pacific coast of Mexico due to the need to maintain

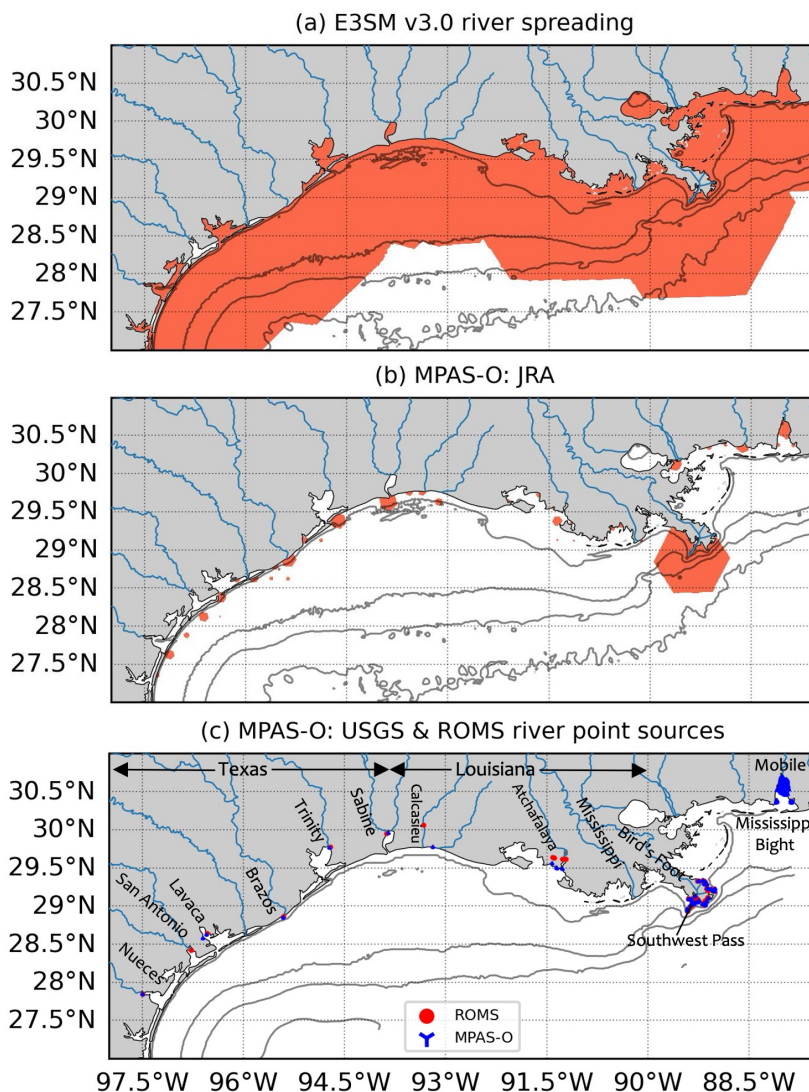


Figure 3. (a) Lateral river spreading in E3SM v3.0 (not used in this study) and (b) MPAS-O: JRA. The red color highlights the lateral spreading of the river volume transport and was saturated for visualization purposes. (c) River point source configuration for ROMS (red dots) and MPAS-O: USGS (blue markers). Other important locations referenced in text are marked in (c). The gray lines are the 10, 50, 100, and 1000 m isobaths, with the MPAS-O isobaths shown in (a-b) and ROMS in (c). Note the Mobile River is included in MPAS-O: USGS but excluded in ROMS.

a continuous global ocean and land mesh, with resolution not able to taper discontinuously. To prevent numerical instabilities, and because there is sufficient geographical separation from the area of interest, these cells were culled from the ocean mesh.



The simulations use a z^* vertical coordinate with partial bottom cells (Petersen et al., 2015). The layer thickness Δz is
 130 calculated as:

$$\Delta z(k) = (\Delta z_{max} - \Delta z_{min}) \tanh \frac{\pi(k - k_0)}{\Delta} + \Delta z_{min}, \quad (1)$$

where k is the layer index, $\Delta z_{max} = 250$ m and Δz_{min} (defined below) are the prescribed maximum and minimum layer thicknesses, respectively, k_0 is the origin in vertical index space of the transition, and $\Delta = 28$ is the number of transition layers over which the tanh function transitions from Δz_{min} to Δz_{max} . The minimum water depth is 5.0 m.

We show results from two simulations that vary in vertical grid, river forcing, and their horizontal mixing coefficients.
 135 The first (MPAS-O: JRA) uses 80 vertical layers with $\Delta z_{min} = 1.0$ m and the second (MPAS-O: USGS) uses 64 layers with $\Delta z_{min} = 0.5$ m (Fig 2). MPAS-O: JRA is intended to be more representative of the model run with parameters and forcing used in fully-coupled climate simulations, whereas MPAS-O: USGS was tuned over a number of six month trial simulations to produce the highest-fidelity result with new river forcing. For example, different vertical grids were used because a trial
 140 simulation with MPAS-O: USGS that used the same vertical grid as MPAS-O: JRA did not produce submesoscale eddies on the shelf (not shown). Trial simulations of six months were used because the plume, although not spun up, develops sufficient eddies during the first summer for preliminary tuning evaluation. Example cross-sections for MPAS-O: USGS and ROMS near Atchafalaya Bay are shown in Fig. 2 (c-d). We refer the reader to Table 1 for a summary of differences between the MPAS-O simulations.

Vertical mixing is parameterized using KPP as part of the CVMix library (Large et al., 1994; Van Roekel et al., 2018). The
 145 model uses harmonic and biharmonic viscosity coefficients scaled to the grid size as:

$$\nu_2^u = \nu_2^0 \left(\frac{\Delta x}{\Delta x_{ref}} \right), \quad (2)$$

$$\nu_4^u = \nu_4^0 \left(\frac{\Delta x}{\Delta x_{ref}} \right)^3, \quad (3)$$

where Δx is the cell width, Δx_{ref} is the reference cell width equal to 30 km, and ν_2^0 and ν_4^0 are the background harmonic and biharmonic viscosities, respectively. These coefficients were tuned to be as small as possible without noise appearing at the grid scale such that ν_2^0 is $66.6 \text{ m}^2\text{s}^{-1}$ for MPAS-O: JRA and $33.3 \text{ m}^2\text{s}^{-1}$ for MPAS-O: USGS. ν_4^0 is $3.33 \times 10^{11} \text{ m}^4\text{s}^{-1}$ for MPAS-
 150 O: JRA and $2.22 \times 10^{11} \text{ m}^4\text{s}^{-1}$ for MPAS-O: USGS. No lateral diffusion is applied to the tracers. Mesoscale eddy effects are parameterized at non-eddying resolutions (> 20 km) using isoneutral diffusion (Redi, 1982) with a constant, slope-limited diffusivity of $300 \text{ m}^2 \text{ s}^{-1}$ and a Gent–McWilliams scheme (Gent and McWilliams, 1990) with the same constant diffusivity. Both coefficients are linearly tapered to zero between horizontal resolutions of 30 km and 20 km. The Fox-Kemper et al. (2011) scheme, which restratifies the upper ocean through submesoscale mixed layer instabilities, is disabled throughout the domain.

155 The simulations employ MPAS-O coupled to MPAS Sea Ice (Petersen et al., 2019; Turner et al., 2022), forced by data-driven atmosphere and river runoff forcings. Coupling to MPAS Sea Ice adds minimal computational cost and was included to account for any potential impacts of sea ice on the representation of the LC. This is implicitly accounted for in the ROMS simulations

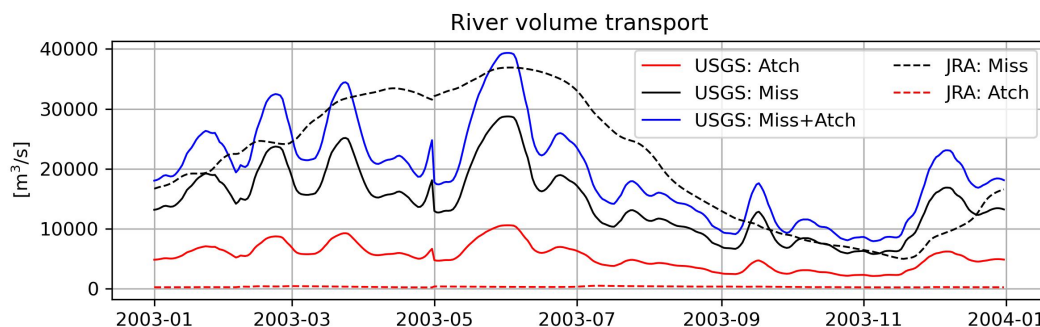


Figure 4. Mississippi and Atchafalaya river volume fluxes calculated from JRA forcing and USGS/USACE streamflow observations. The sharp transition on Apr. 30 is a result of RYF.

through the global HYCOM open boundary forcing, which is data assimilative. The simulations use the same atmospheric forcing as the ROMS model. MPAS-O uses a kinematic surface boundary condition for volume conservation.

160 In E3SM v3.0, river runoff fluxes are prescribed daily from the 0.25° JRA river discharge dataset (Suzuki et al., 2018). External mapping files are used to spread river runoff (Golaz et al., 2025) horizontally and the vertical distribution of river runoff follows an exponential decay of the form $\exp(z/0.75)$. The Jerlov water type is set to three everywhere. The magnitude of the horizontal spreading, which is applied in the same way for each river, was originally dictated by Amazon River outflow stability requirements. This resulted in river fluxes being spread hundreds of kilometers offshore (Fig. 3a) and was not tested
 165 here. In future versions of E3SM, the spreading distance will be proportional to the inflowing runoff fluxes of each river (Fig. 3b) using a Gaussian distribution whose length scale is determined by both the maximum runoff flux found in JRA forcing and the local grid scale. River runoff is initially located at the ocean grid cell that is nearest to the location specified by the runoff data.

In this study, we used this newer spreading in the MPAS-O: JRA simulation to understand the model’s strengths and limita-
 170 tions when used in a way typically designed for global ocean studies. For example: (1) much of the river water is still spread over the 100 m isobath where it often exits the shelf permanently (Zhang et al., 2012a, 2014), (2) the spreading distributes Miss. River water primarily along the western edge of Bird’s foot, whereas the ROMS model and observations suggests the rates are closer to 64% (Sorourian et al., 2022), with the remainder distributed around several other passes to the northeast (Fig. 3c), (3) many river discharge points are spuriously placed in the open ocean by the remapping file, and (4) JRA forcing does not
 175 account for the USACE’s Old River Control structure that diverts roughly 30% of the Miss. River water to the Atchafalaya (Fig. 4). As a result, the Atchafalaya River volume fluxes are severely underestimated, which contributes to major salinity biases on the shelf (see § 3.3).

In the MPAS-O: USGS simulation, we used the same JRA river spreading and forcing as in the MPAS-O: JRA simulation outside of the ROMS model domain. Inside the ROMS domain, the JRA river flux is set to zero and replaced by what we are
 180 calling “pseudo point sources” that result in a substantially more realistic river configuration in the nGoM (Fig. 3c). These



are the fluxes and locations specified by the USGS streamflow data used in the ROMS simulations interpolated to the nearest MPAS-O grid cell. We refer to them as pseudo point sources, as the horizontal momentum fluxes associated with the river discharge is still zero, which may significantly alter dynamics in the M-A plume's near-field. There are some small mismatches in the locations of the ROMS point sources and the MPAS-O: USGS pseudo point sources (Atchafalaya, Calcasieu, San Antonio) due to differences in model bathymetry and interpolation discrepancies.

In E3SM v3.0, river runoff temperatures are set equal to the sea surface temperature of the nearest ocean cell. As explicit river temperatures are not yet available from the river model (MOSART), this approach was chosen in the interim in E3SM to preserve energy conservation in fully-coupled simulations. While this nearest-neighbor approach has little impact in coarse-resolution, fully coupled climate simulations, it is problematic in the northern Gulf of Mexico (nGoM), where river temperatures during summer are often cooler than the surrounding ocean. In MPAS-O: JRA trial simulations, this treatment produced spurious temperature spikes at the Mississippi River mouth that could not be corrected by adjusting runtime parameters. To address this, and because energy conservation is not a constraint in the ocean and sea ice only simulations used here, we implemented an option to set river temperatures equal to the 10 m JRA air temperature, with an upper limit of 30°C, keeping river temperatures consistent with observations and ROMS model inputs. This feature is applied to all rivers in both MPAS-O: JRA and USGS simulations. While it substantially improved temperature fidelity in the nGoM relative to the original E3SM v3.0 approach, it likely reduced accuracy in polar regions but is neglected due to the short simulation length. A geographically based hybrid approach will be explored in future work.

The simulations were run on 5120 cores (one node has 128 cores) at Los Alamos National Laboratory Institutional Computing, with 4864 cores used for MPAS-O and 256 cores used for MPAS Sea Ice. MPAS-O: JRA achieved approximately 0.4 SYPD and MPAS-O: USGS achieved roughly 0.5 SYPD. Snapshots and averages of two dimensional variables were saved every 12 hours, whereas three dimensional variables were saved weekly. MPAS-O: JRA was run for four years to conserve computational resources because it did not produce realistic shelf eddies (discussed in § 3.2). Analysis of model output was done from years three through four. MPAS-O: USGS was run for five years and analysis of model output was done from years three through five.

205 3 Results

3.1 Submesoscales in the open GoM

We start with an overview of MPAS-O's representation of submesoscales in the open GoM. Fig. 5 shows winter and summer snapshots of normalized relative vorticity $\zeta f^{-1} = (\partial_x v - \partial_y u) f^{-1}$ for MPAS-O: JRA. Consistent with previous studies (Barkan et al., 2017b; Bracco et al., 2019; Liu et al., 2021; Ntaganou et al., 2024), submesoscales form almost everywhere in winter in the GoM, including within and around LC eddies, on the continental shelves, and near river outflow sources. "Submesoscale soup", consisting of chaotic fronts, filaments, and instabilities, is prominent on the continental shelves. It is only partially resolved at 1.5 km resolution, as the mixed layer deformation radius is $\mathcal{O}(0.5-5 \text{ km})$ (Barkan et al., 2017b). The impacts of resolution on the dynamics is apparent, as much of the Gulf Stream and Northwestern Atlantic lies within the

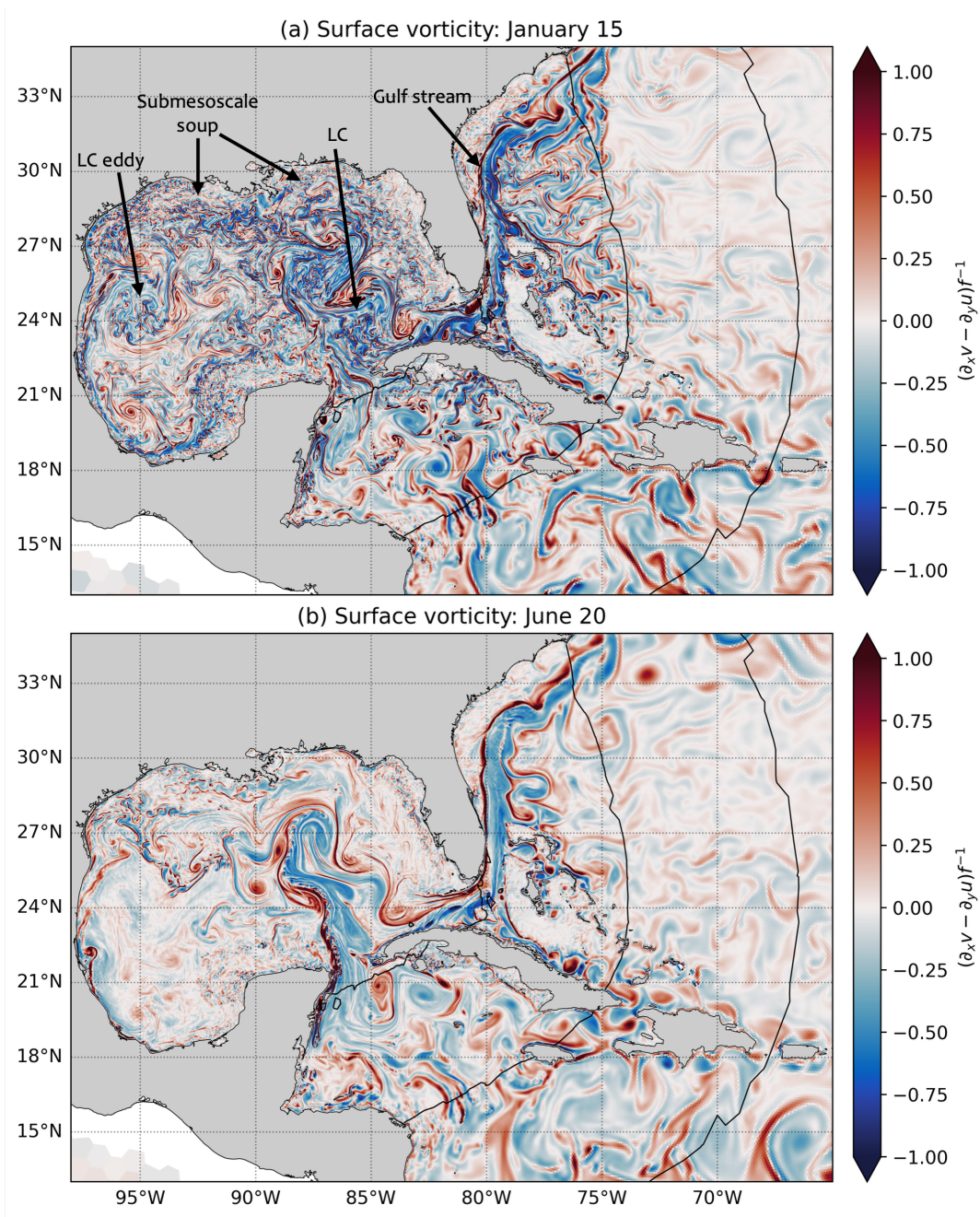


Figure 5. MPAS-O: JRA ζf^{-1} snapshots during (a) winter and (b) summer of year three. The black contours mark 1.5, 5, and 10 km horizontal resolutions. The LC eddy in (a) is confirmed using sea surface height anomalies and is not shown.

transition zone between 1.5- and 10 km resolutions. As expected, submesoscale prominence and abundance decreases with
215 decreasing horizontal resolution.

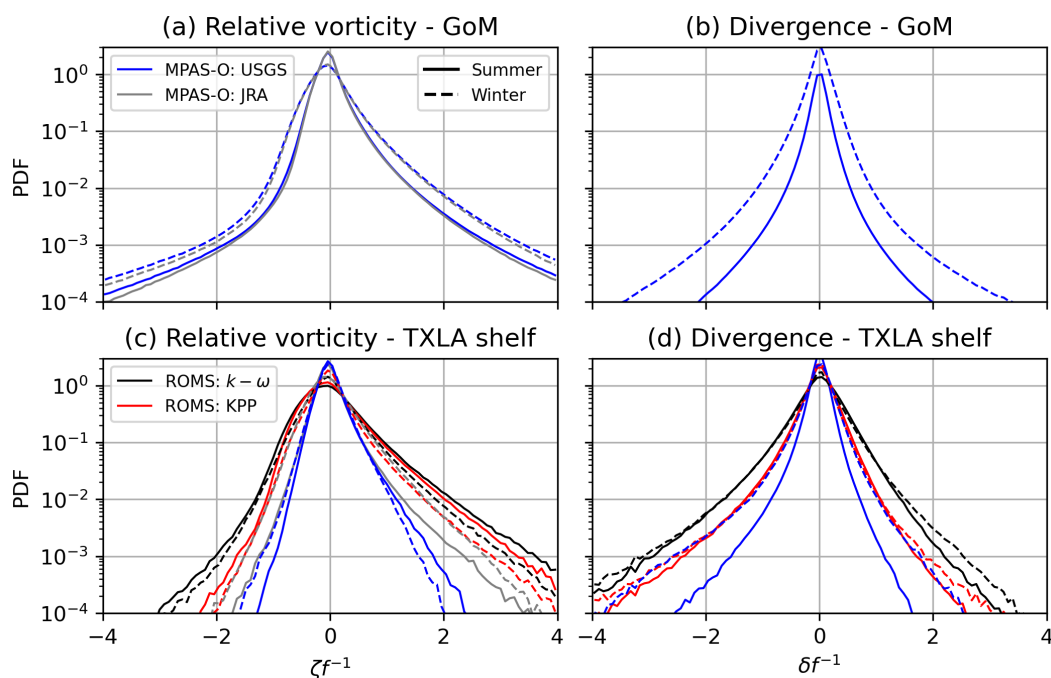


Figure 6. PDFs of (a) ζf^{-1} and (b) δf^{-1} for the MPAS-O simulations inside the entire GoM during summer (JJA, solid lines) and winter (DJF, dashed lines). (c-d) Same as (a-b), but on the TXLA shelf inside the magenta box shown in Fig. 1 for the 4 simulations. Note that δf^{-1} for MPAS-O: JRA (in b,d) is not shown due to a file corruption issue.

The generation and seasonality of submesoscales depends on location because they are controlled by lateral density gradients (McWilliams, 2016; Taylor and Thompson, 2023), which is influenced by M-A River discharge (Barkan et al., 2017b, a) and LC eddies. In the open GoM where the dynamics are temperature-driven, submesoscales are primarily generated by mixed layer instabilities and are more abundant in winter and suppressed in summer (Luo et al., 2016). This is closely tied to mixed layer depth, which increases in winter and thus increases the amount of potential energy that can be extracted from lateral density gradients (Callies et al., 2015; Luo et al., 2016). In summer, increased solar heating shoals the mixed layer and reduces the strength of mixed layer instabilities. M-A River discharge has a complex and seasonal influence on submesoscales in the open GoM (Barkan et al., 2017b, a). River discharge in all seasons can enhance lateral density gradients and serves as a key driver of submesoscale generation via frontogenesis despite the suppression of mixed layer instabilities. In winter, the M-A rivers can enhance or suppress mixed layer instabilities depending on the interplay between stratification and mixed layer depth.

Submesoscale variability in the open GoM is also shown with probability density functions (PDFs) of surface normalized relative vorticity (Fig. 6a,c) and divergence $\delta f^{-1} = (\partial_x u + \partial_y v) f^{-1}$ (Fig. 6 b,d). The skewness of these PDFs are hallmarks of abundant submesoscale activity (Balwada et al., 2021; Shcherbina et al., 2013). The relative vorticity PDFs are positively

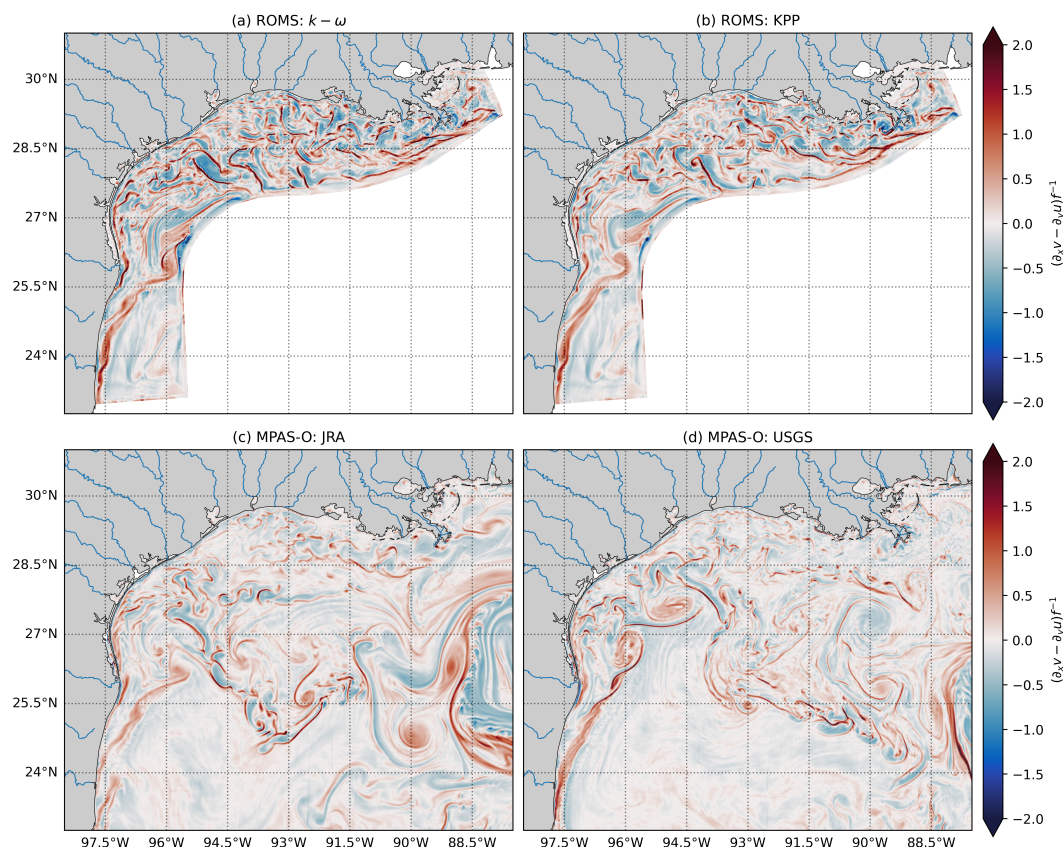


Figure 7. Zoom in of ζf^{-1} snapshots for (a) ROMS: $k - \omega$, (b) and ROMS: KPP, (c) MPAS-O: JRA, and (d) MPAS-O: USGS. Time is the same as Fig. 5 (b), but note the difference in colorbar range.

230 skewed (towards cyclonic vorticity) in both seasons (Fig. 6a), with the distributions qualitatively similar between the MPAS-O simulations. In winter, the tails are further elongated, indicating stronger anticyclonic eddies and higher levels of frontogenesis. The divergence PDFs are negatively skewed (towards convergence) in both seasons, but the distribution widens more in winter than summer compared to relative vorticity. We leave a more detailed analysis of submesoscale dynamics in the open GoM to future work, as the primary focus of this study is on the M-A plume.

235 3.2 Suppression of TXLA shelf eddies in MPAS-O

We start with an analysis of the ROMS simulations because the model statistically reproduces the characteristics of TXLA shelf eddies (Kobashi and Hetland, 2020). As discussed in § 1, shelf eddies are more prominent in summer than winter due to changes in regional wind patterns that reduces overall submesoscale activity (Hetland, 2017; Zhang et al., 2012a, 2014). An example of the eddies can be seen in plan view plots of surface relative vorticity (Fig. 7a-b). While both ROMS simulations are qualitatively similar, the ROMS: KPP simulation is slightly smoother at the grid scale than ROMS: $k - \omega$.

240



The seasonality of submesoscales is also reflected in the PDFs of relative vorticity on the inner shelf (0-50 m depth, see Fig. 1b–c for location) for the ROMS simulations (Fig. 6c), where the distributions narrow slightly in winter relative to summer. Note that we focus on the inner shelf because circulation there is primarily wind-driven, in contrast to the outer shelf where LC eddy interactions play a larger role (Zhang et al., 2012a). Consequently, differences between MPAS-O and ROMS on the inner shelf primarily reflect each model’s ability to represent the M–A plume, rather than differences caused by the representation of LC eddies between MPAS-O and HYCOM (used for the ROMS open boundary forcing).

PDFs of divergence (Fig. 6d) on the inner shelf exhibit the opposite trend, where the distributions broaden in winter, but not nearly as much as the open GoM. This result has not been shown in previous studies and we hypothesize this is due to increased wind forcing (Kobashi and Hetland, 2020), which enhances frontogenesis and leads to more intermittent, spatially localized convergence and divergence. This requires further investigation but is beyond the scope of this paper. ROMS: $k - \omega$ has the broadest distribution of the four simulations for both variables. ROMS: KPP has narrower distributions than ROMS: $k - \omega$. We attribute this to ROMS: KPP being more diffusive. An example of this elevated diffusion is shown in Fig. 8 and discussed below.

A key result is that the MPAS-O simulations (Fig. 7c-d) do not produce a submesoscale eddy field with the same realism or qualitative characteristics as the ROMS simulations (Fig. 7a-b). The MPAS-O simulations produce organized meanders on the Texas shelf (e.g., west of 93.5°W) but they have weaker relative vorticity than the ROMS model and lack the same complexity. This is especially true on the Louisiana Shelf for MPAS-O: USGS. Surprisingly, MPAS-O: USGS features less submesoscale activity than MPAS-O: JRA near the M-A river mouths and on the Louisiana shelf despite improved river forcings, increased minimum layer thickness, and reduced horizontal mixing.

This is also shown in PDFs of relative vorticity (Fig. 6c), where both MPAS-O simulations have narrower distributions than the ROMS simulations, with MPAS-O: USGS having the smallest distribution for both seasons. Because realistic eddies do not form in these simulations, the interpretation of seasonal differences in MPAS-O’s PDFs is substantially complicated. For example, MPAS-O: JRA has a broader relative vorticity distribution in winter rather than summer that is nearly identical to ROMS: KPP. On the other hand, MPAS-O: USGS has a larger anticyclonic tail in winter, but is narrow in summer. However, the divergence PDF for MPAS-O: USGS is similar to ROMS: KPP during winter but is substantially weaker in summer than the other simulations.

Fig. 8 shows cross-sections of salinity (a,c,e) and vertical eddy viscosity ν_v (b,d,f) west of Atchafalaya Bay averaged over June of year four, for MPAS-O: USGS and the ROMS simulations. The cross-sections are located in the plume’s far-field, defined as the region where the plume has lost all memory of inflowing momentum fluxes (Horner-Devine et al., 2015). The surface boundary layer depth is shown for MPAS-O: USGS (Fig. 8a-b) and ROMS: KPP (Fig. 8c-d) because it is the fundamental diagnostic that controls the extent of nonlocal turbulent mixing. In MPAS-O: USGS, a brackish lens forms in the top several meters of the water column that is absent in the ROMS simulations. The mean boundary layer depth for MPAS-O: USGS is 3.3 m and 3.4 m for ROMS: KPP, but the two may differ by over a meter locally. Values of ν_v are generally smaller in MPAS-O: USGS, except in the ocean interior where the default to prescribed background levels (10^{-5} for ROMS: KPP, 10^{-4} for MPAS-O: USGS). Within the boundary layers, ν_v in ROMS: KPP can exceed MPAS-O: USGS by over an

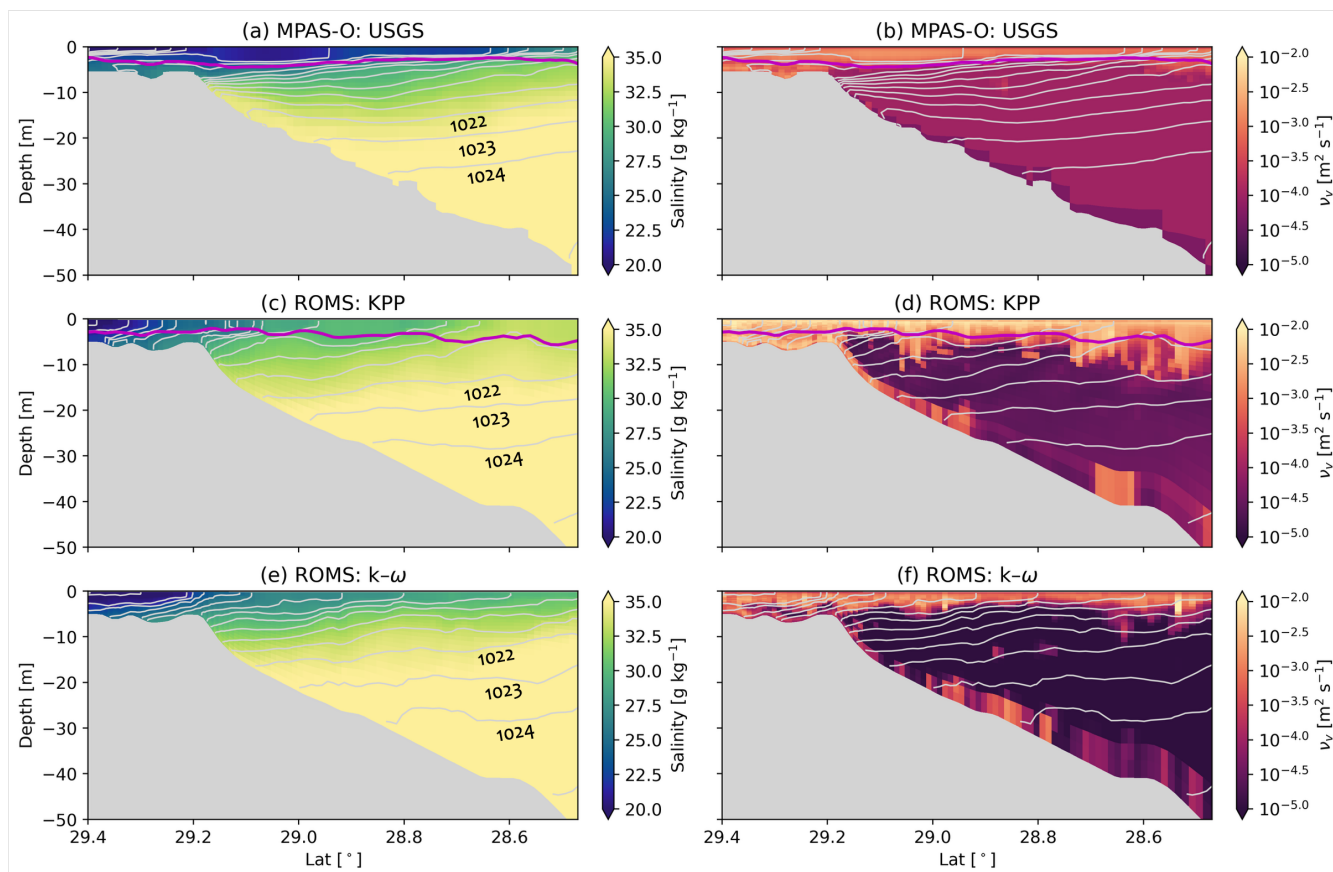


Figure 8. Cross-sections of salinity and vertical eddy viscosity. (a–b) MPAS-O: USGS, averaged over June of year 4, (c–d) ROMS: KPP, and (e–f) ROMS: $k-\omega$. Isopycnals are overlaid in gray at 1 kg m^{-3} intervals and the surface boundary layer depth is shown with the magenta lines. The cross-section location is the same as in Fig. 2. Note that the boundary layer depth is only available for ROMS: KPP because it is calculated online at every timestep, unlike when $k-\omega$ is used. See McWilliams et al. (2009) for more information.

order of magnitude. We note that MPAS-O: USGS demonstrates weaker mixing close to the seafloor relative to ROMS: KPP because CVMix lacks an explicit bottom boundary layer parameterization. In ROMS: KPP, we use a bottom boundary layer parameterization that is analogous to the surface boundary layer parameterization. The salinity and ν_v sections for ROMS: $k-\omega$ (Fig. 8e–f) are similar to ROMS: KPP, but ROMS: KPP is generally more diffusive. These trends are also confirmed in PDFs of ν_v computed over the same region as in Fig. 6 (not shown). It remains unclear to what extent the reduced vertical viscosity—and therefore weaker vertical mixing (i.e., destruction of scalar variance)—is a cause of eddy suppression, a consequence of eddy suppression, or how different configuration choices contribute to these behaviors. For example, the CVMix implementation of KPP has not been tuned for coastal buoyancy-driven flows and differs in several respects from ROMS’ native KPP scheme (Li et al., 2019). We discuss how various configuration choices could contribute to eddy suppression in §4.



285 3.3 MPAS-O's representation of the larger-scale TXLA shelf circulation

The objective of this section is to understand how eddy suppression affects MPAS-O's ability to represent the larger-scale circulation and seasonal evolution of the M-A plume. We are also interested in comparing the bulk transport and fate of M-A plume water between models. One tool that accomplishes both simultaneously is an analysis of freshwater dyes following Zhang et al. (2012a), who used an earlier version of the ROMS model to investigate freshwater transport on the TXLA shelf.

290 For all simulations except MPAS-O: JRA, the M-A rivers are tagged using passive dyes ϕ with an initial concentration of one at the point sources and zero elsewhere. A concentration of one means a parcel consists of purely river water, whereas a parcel with a concentration of zero has no river water. We omitted this feature when running MPAS-O: JRA for two reasons: (i) the Atchafalaya River fluxes dramatically differ from streamflow observations (Fig. 4), and (ii) the river spreading scheme for the Mississippi instantaneously deposits freshwater offshore of how the shelf freshwater volume is defined. Thus, we did not
 295 expect an analysis of MPAS-O: JRA to be meaningful relative to the other simulations, even if by coincidence the freshwater volume ended up being similar.

We define the freshwater volume V_f for each river as:

$$V_f = \iint_{\Omega_b} \left(\int_{H > -100}^{\eta} \phi(x, y, z, t) dz \right) dx dy, \quad (4)$$

where Ω_b denotes the lateral boundaries of the ROMS model domain, η is the sea surface height, and ϕ is the dye concentration in each grid cell. We note that the domain volume inshore of the 100 m isobath is approximately 4.4% smaller in ROMS than
 300 MPAS-O due to differences in bathymetry and the culling of land cells during the MPAS mesh generation process. Time series of V_f with the river volume fluxes overlaid for the simulations are shown in Fig. 9. After two years, the freshwater volume for both rivers in the ROMS simulations show a clear seasonal cycle with little day of year variability (for the ROMS simulations), confirming the two year spinup time discussed in § 2.1.

V_f is strongly correlated with river discharge; higher discharge corresponds to higher V_f (Zhang et al., 2012a). Previous
 305 studies have shown that the eddies are the dominant mechanism for transporting material off the shelf (Hetland, 2017; Thyng and Hetland, 2018; Zhang and Hetland, 2018; Zhang et al., 2014). Given that these simulations have the same river discharge inside the ROMS domain, we primarily attribute a larger larger V_f to reduced submesoscale activity. Differences in LC dynamics, held constant with respect to day of year in ROMS due to the open boundary forcing (unlike MPAS-O), may also influence model differences in freshwater content because LC eddy interactions influence the circulation between 50-100 m
 310 depth (Zhang et al., 2012a).

Mississippi River discharge (Fig. 9a) peaks in late March and early June and generally decreases until late November. For the ROMS simulations, V_f is higher in late spring and early summer, peaking in July. Trends are similar for the Atchafalaya (Fig. 9b). For ROMS: $k - \omega$, the maximum correlation between the Mississippi discharge and the freshwater volume is 0.84, which occurs with a 39 day lag (discharge leads volume). The maximum correlation for the Atchafalaya is 0.75, also with a
 315 39 day lag. Results are similar for ROMS: KPP, however the freshwater volume associated with each river are slightly higher than ROMS: $k - \omega$ (4% for the Mississippi, 10% for the Atchafalaya). Thus, it takes over a month for freshwater discharge to

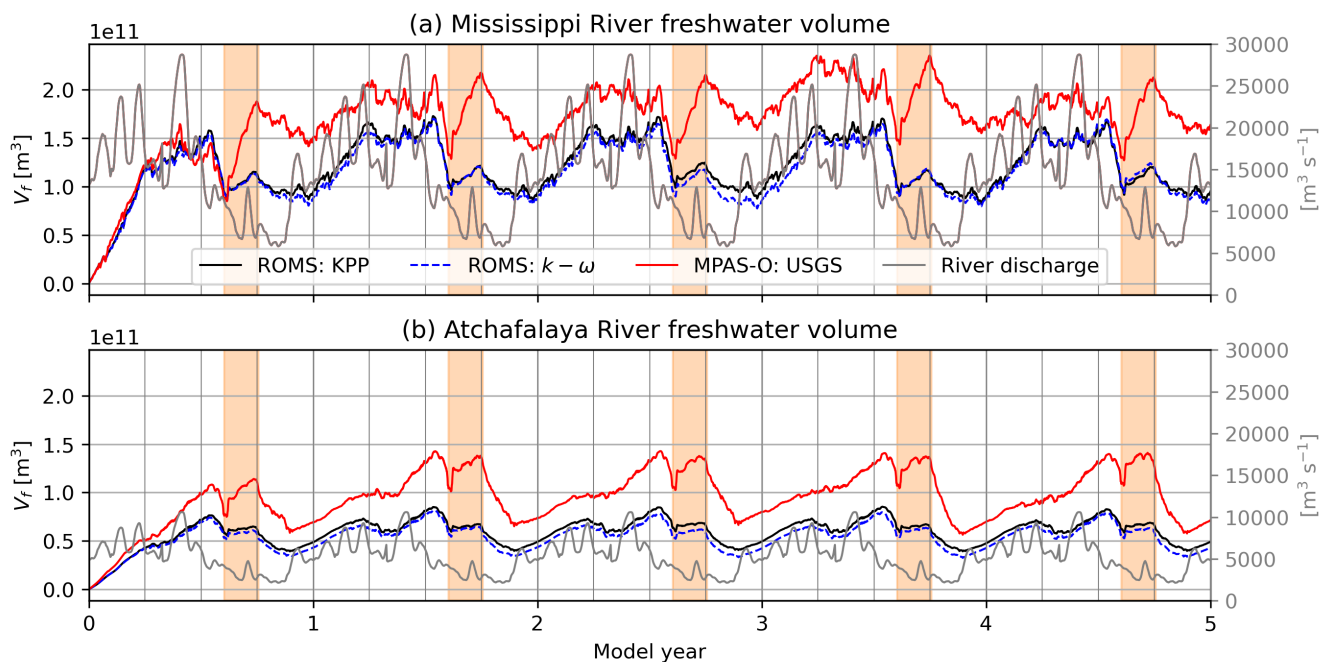


Figure 9. Time series of freshwater volume V_f for the (a) Mississippi and (b) Atchafalaya Rivers. The gray lines show volume fluxes for each river. The shaded orange boxes are from Aug 8 - Oct 3 of each year to highlight significant increases in MPAS-O's freshwater volume that are absent in the ROMS simulations.

interact with the continental shelf before it is possibly exported to open water. We note that Zhang et al. (2012a) performed a similar analysis from 2005-2011 and found similar values for the correlation coefficients, but with lags of 21 days for the Mississippi and 33 days for the Atchafalaya. We attribute this to reduced summer eddy activity for 2003-2004 relative to other years, which can be confirmed by comparing PDFs of surface vorticity (compare Fig. 6 to Fig. 3 of Schlichting et al. (2023)).

MPAS-O: USGS qualitatively captures the seasonal evolution of the freshwater volume for both rivers. However, the time-averaged freshwater volume is 42% higher than the ROMS: $k - \omega$ for the Mississippi and 58% higher for the Atchafalaya. In summer, the freshwater volume for MPAS-O: USGS may occasionally be over twice that of the ROMS simulations. The freshwater volume is also more variable year over year in MPAS-O: USGS than the ROMS simulations. This could be due to internal variability in LC dynamics within MPAS-O, whereas LC effects are implicitly represented and held constant from year to year in the open-boundary forcing of the ROMS simulations. As a result, correlations between discharge and freshwater volume are lower in MPAS-O: USGS, with a maximum correlation of 0.32 between Mississippi discharge and volume with a 41 day lag. For the Atchafalaya, the maximum correlation is 0.53 with a 56 day lag. This analysis indicates that MPAS-O has much more freshwater on the shelf than ROMS. It also takes longer for freshwater to leave the shelf in MPAS-O, especially for the Atchafalaya.



In addition, there are peaks in MPAS-O: USGS freshwater volume in late summer and early fall that are absent in the ROMS simulations. These peaks occur several weeks after increases in M-A river discharge and intense downcoast winds (not shown). There is a strong northward return flow on the western Texas shelf not present in the ROMS simulations (e.g., 96°W, 23-27°N) and several mesoscale features that appear to be the cause of this excessive freshwater accumulation. This can be interpreted with the help of a supplementary plan view animation of seasonally-averaged M-A freshwater thickness h and transport Q for MPAS-O: USGS and ROMS: $k - \omega$ (see Code and Data Availability), which we define as:

$$h = \int_{-H}^{\eta} \phi dz, \quad (5)$$

$$Q = \int_{-H}^{\eta} \mathbf{u}_h \phi dz, \quad (6)$$

where \mathbf{u}_h is the horizontal velocity vector.

Plan view plots of seasonally-averaged freshwater thickness and transport (Fig. 10) show that MPAS-O: USGS qualitatively reproduces the extent of the plume and the direction of freshwater transport. Consistent with the freshwater volume, both freshwater thickness and transport may be several times larger in MPAS-O than ROMS: $k - \omega$ locally. For both models, the plume is confined closer to the coast and extends southward toward the Mexico border in winter (Fig. 10a-b). In summer (Fig. 10c-d), the plume shifts northward and spreads over the shelf. Both models contain several similar features on the inner shelf, including (i) a recirculating bulge west of Bird's Foot, which has been extensively documented (Wiseman et al., 1997; Hetland, 2017), (ii) a persistent mesoscale gyre near 94°W in summer, which is also visible in surface snapshots of relative vorticity (Fig. 7b), and (iii) the largest freshwater transport generally occurs near the M-A river mouths, consistent with Zhang et al. (2012a). The freshwater thickness is larger in MPAS-O: USGS than the ROMS simulations on most of the shelf.

On the continental slopes (see red lines in Fig. 10), model differences are more dramatic and highlight a limitation of using a limited-domain model. In ROMS, the freshwater thickness and transport is smaller year round. This is likely due to the radiation boundary conditions and the climatological nudging layer, which relaxes the passive dyes to zero over the first 10 interior grid points. Thus, we do not expect the behavior of the ROMS model to be realistic close to the open boundaries. Despite the lack of shelf eddies, a major advantage of MPAS-O is that it can be used to study the fate and transport of M-A river water into the open GoM. For example, the imprint of M-A river water is apparent as far south as 22°N and on the Florida shelf, interacting with the LC and numerous mesoscale features. It can also be seen in the Gulf Stream (not shown). An interesting result is that the freshwater transport in the LC eddies can exceed the transport on much of the shelf, likely due to the energetic surface currents.

Finally, we compare the surface tracer fields between the simulations using summer (Fig. 11) and winter (Fig. 12) averages of sea surface salinity (SSS) and temperature (SST). The 33 g kg⁻¹ isohaline, which is the operational plume boundary (Hetland and Hsu, 2013; Kobashi and Hetland, 2020), and the 100 m isobath, are shown in the SSS panels (Figs. 11-12a-d). These complement the freshwater analysis by highlighting the seasonal variability of the plume extent in a different way. Differences between ROMS: $k - \omega$ SSS and the MPAS-O simulations (Δ SSS) are shown in Figs. 11- 12 e-f with MPAS-O fields interpolated

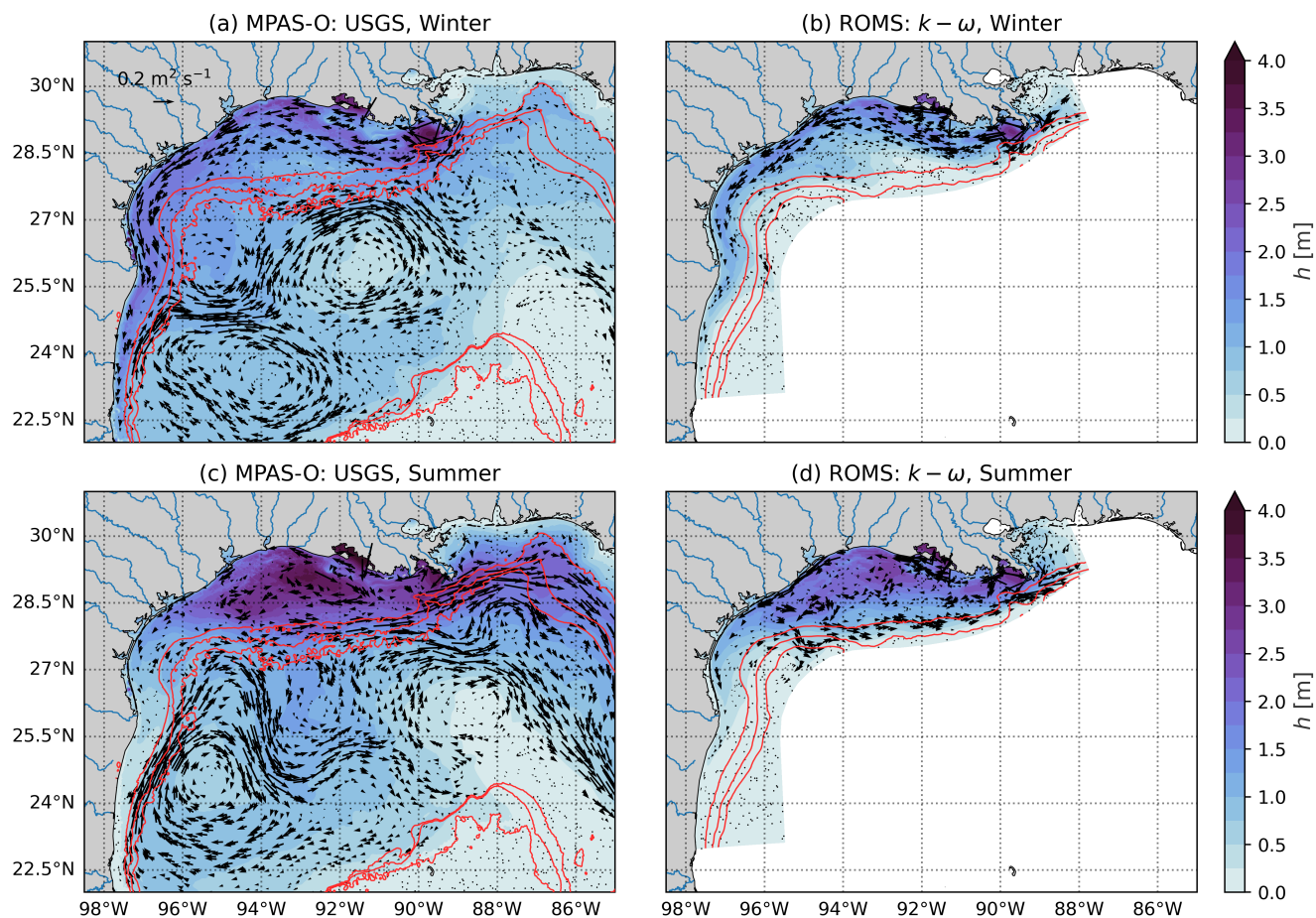


Figure 10. Plan view plots of combined freshwater thickness and flux vectors for the M-A Rivers for MPAS-O: USGS and ROMS: $k - \omega$ during (a-b) winter and (c-d) summer, respectively. The red lines mark the 100, 500, and 1000 m isobaths to emphasize the continental slopes. The ROMS: KPP simulation is similar to ROMS: $k - \omega$ and is not shown.

365 onto the ROMS grid using Delaunay triangulation. On the Louisiana shelf, ROMS: $k - \omega$ is significantly fresher than MPAS-O: JRA ($\Delta SSS < -9 \text{ g kg}^{-1}$; Fig. 11e) due to the underestimation of Atchafalaya River discharge. The imprint of MPAS-O: JRA's river spreading is visible in both the SSS (Fig. 11a) and the ΔSSS fields (Fig. 11e). ROMS is saltier north of the Mississippi delta because brackish water from Lake Pontchartrain and the Mobile River is excluded. Qualitatively, ROMS: $k - \omega$ more closely resembles MPAS-O: USGS than JRA on the Louisiana shelf but is saltier almost everywhere. SST is relatively uniform on the shelf in summer (Fig. 11g-j). As a result, the differences between ROMS: $k - \omega$ and both MPAS-O simulations (ΔSST) are approximately $\pm 1.5^\circ\text{C}$ despite the lack of eddies in MPAS-O (Fig. 11k-l). ROMS: $k - \omega$ is slightly warmer ($\Delta SST < 0.5^\circ\text{C}$) than both MPAS simulations, except close to the river discharge points, likely due to differences in how river temperatures are prescribed (see § 2).

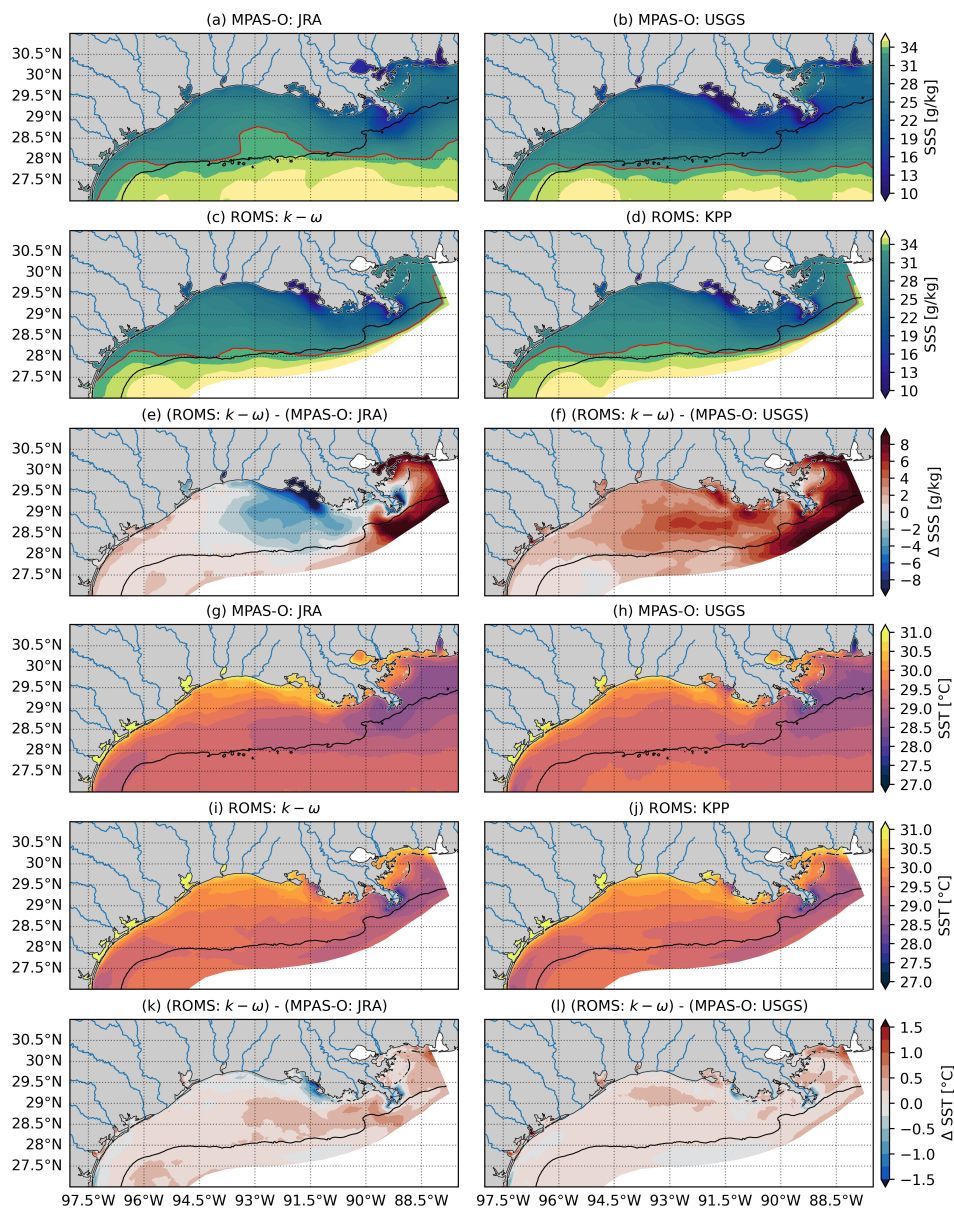


Figure 11. (a-d) Sea surface salinity (SSS) averaged over summer for the 4 simulations. In (a), SSS output from years 3-4 is used. In (b-d), SSS output from years 3-5 is used. The black line marks the 100 m isobath and the red line marks the 33 g kg^{-1} isohaline, the boundary of the M-A plume. Note that SSS plots use a colormap constructed with piecewise linear normalization about $\text{SSS}=33 \text{ g kg}^{-1}$ to emphasize plume versus oceanic water. (e) SSS difference between ROMS: $k - \omega$ and MPAS-O: JRA interpolated onto the ROMS grid. (f) Same as (e), but for the MPAS-O: USGS simulation. (g-l) Same as (a-f), but for sea surface temperature (SST).

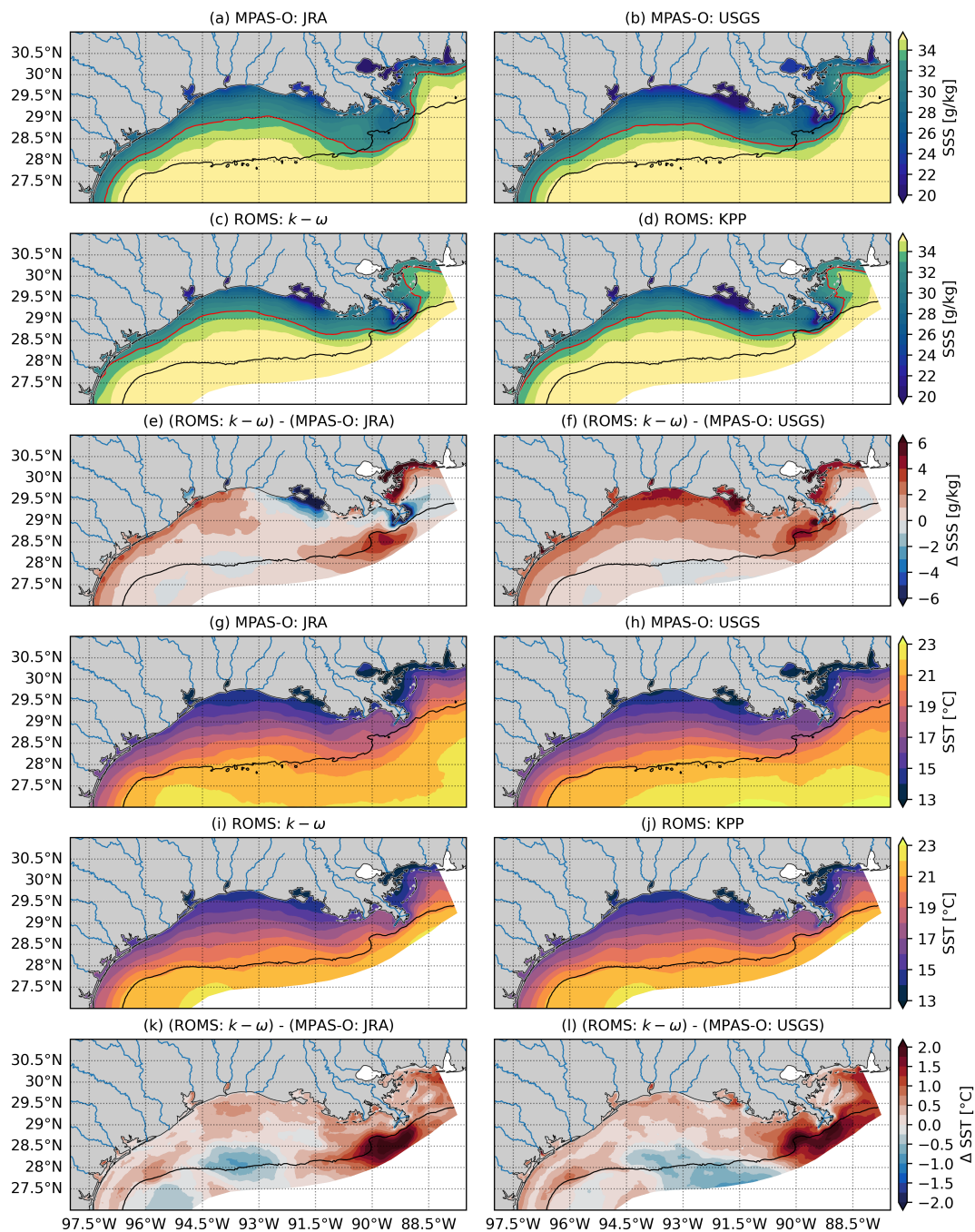


Figure 12. (a-d) Same as Fig. 11, but for winter. Note the difference in colorbar range.



370 In winter, the salinity fields and plume boundary between MPAS-O and ROMS are more similar due to eddy suppression. The shelf becomes saltier as the plume is confined closer to the coast (Fig. 12a-d). As a result, ΔSSS shrinks (Fig. 12e-f), with ROMS: $k - \omega$ remaining fresher than MPAS-O: JRA near Atchafalaya Bay ($\Delta SSS < 6 \text{ g kg}^{-1}$). The opposite is true for MPAS-O: USGS, with it being fresher than ROMS: $k - \omega$ ($\Delta SSS < -6 \text{ g kg}^{-1}$) near Atchafalaya Bay. As the SST distribution broadens (Fig. 12g-l), ΔSST increases to over 2°C southwest of Bird's Foot for both MPAS-O simulations, but
375 is smaller almost everywhere else. These results suggest MPAS-O demonstrates increased performance in winter when eddies are naturally suppressed despite elevated freshwater content from the previous summer influencing the results.

4 Discussion and conclusions

Previous studies with unstructured grid models have shown promise in their ability to seamlessly integrate coastal processes with the global circulation (Mathis et al., 2022; Zhang et al., 2023). However, none have focused on coastal submesoscale
380 dynamics. Here, we have assessed an unstructured global model's ability (MPAS-O) to represent submesoscale dynamics using regional refinement. Encouraged by MPAS-O's performance in idealized simulations in Part I (Hinson et al., 2026), we focused on the Texas–Louisiana (TXLA) shelf in the northern Gulf of Mexico (nGoM). This region is strongly influenced by discharge from the Mississippi and Atchafalaya (M-A) Rivers and regional winds. The defining dynamical feature of this region is a submesoscale eddy field that forms during summer in response to weakly upcoast winds (Hetland, 2017; Qu et al.,
385 2022). During non-summer months, winds become downcoast and increase in intensity, suppressing the eddy field and causing submesoscales to behave more as “submesoscale soup” (Hetland, 2017).

To assess MPAS-O's fidelity, we compared two simulations, MPAS-O: JRA and MPAS-O: USGS, against a validated limited-domain ROMS model (Kobashi and Hetland, 2020; Zhang et al., 2012b). All simulations used repeat year forcing (RYF) from 2003-2004 to isolate differences caused by model physics, numerics, and parameterizations. The MPAS-O simu-
390 lations differed in their treatment of river runoff, vertical resolution, and explicit lateral mixing coefficients. With the exception of the horizontal grid, the configuration for MPAS-O: JRA is more similar to how MPAS-O is configured for coarser-resolution fully-coupled simulations. For example, MPAS-O: JRA uses external mapping files to laterally spread river runoff where the spreading distance is proportional to the magnitude of the river runoff fluxes (Fig. 3b). The source of river runoff fluxes, Japanese Reanalysis (Stewart et al., 2020), underestimates Atchafalaya River discharge by over an order of magnitude (Fig. 4)
395 compared to streamflow observations. In MPAS-O: USGS, rivers are configured as “pseudo” point sources within the ROMS domain such that the locations of the rivers into the ROMS domain are interpolated onto the MPAS grid. Likewise, MPAS-O used the same streamflow data as ROMS within the ROMS model domain and JRA streamflow elsewhere. However, trial simulations (not shown) that used the same vertical grid and explicit lateral mixing parameters as MPAS-O: JRA did not produce a realistic eddy field. In an attempt to alleviate this, we used a higher resolution vertical grid with 0.5 m thick layers (half
400 that of MPAS-O: JRA) and tuned the explicit lateral mixing to be as small as possible, yet eddies remained suppressed. As a result, MPAS-O: USGS has excessive freshwater relative to ROMS on the inner shelf year round, causing significant salinity ($\mathcal{O}(10 \text{ g kg}^{-1})$) differences. The plume also extends much further offshore in MPAS-O: USGS in summer relative to the



ROMS simulations. We attribute this behavior in ROMS to the climatological nudging to HYCOM at the open boundaries. By the same metrics, MPAS-O's performance is improved during winter when eddies are naturally suppressed. Thus, a primary
405 finding of this study is that MPAS-O needs significant exploration and improvement to operate well in coastal domains.

An unsatisfying result is that the suppression of TXLA shelf eddies in MPAS-O likely arises from interacting numerical and parameterization choices whose combined effects are difficult to disentangle. We speculate on likely and unlikely causes because we hope this will be useful for the community and to future studies. We observe that MPAS-O: USGS develops a persistent brackish lens in the upper 5 m of the water column (Fig. 8a,c,e), even in the plume far-field, which is associated
410 with weaker boundary layer vertical viscosity relative to the ROMS base case (ROMS: $k-\omega$). A plausible explanation is that the CVMix implementation of the K-Profile Parameterization (KPP; Van Roekel et al., 2018) requires substantial tuning. It contains numerous adjustable parameters and the behavior can vary substantially across models and within a single model with variable resolution (Li et al., 2019; Van Roekel et al., 2018). A ROMS simulation employing its native KPP implementation (ROMS: KPP) generates shelf eddies comparable to ROMS: $k-\omega$, despite exhibiting stronger viscosity than either ROMS: $k-\omega$
415 or MPAS-O: USGS (Fig. 8).

The idealized simulations in Part I showed that vertical mixing in MPAS-O was higher than ROMS. A key detail, however, is that in the idealized model, a vertically uniform lateral salinity gradient is imposed initially and evolves freely through mixed-layer instability, with no ongoing buoyancy source. In the realistic simulations, the M-A plume is continuously forced by riverine freshwater input, which maintains spatially heterogeneous surface density gradients that are sharpened by winds.
420 Thus, the contrasting forcing regimes complicate direct attribution of the suppressed eddy activity to vertical mixing differences alone. A clear direction for future work would be to add river forcing to the idealized model. However, MPAS-O does not have the capability to apply river forcing in idealized domains and adding this capability is beyond the scope of this study.

Neglecting horizontal momentum associated with river runoff might alter the plume structure near freshwater sources. This likely reduces the lateral shear along the plume front, which could indirectly diminish vertical shear and might contribute to
425 reduced mixing. This may explain why MPAS-O remains much fresher close to the river mouths. Yet, the neglect of horizontal momentum should be localized to the plume's near-field and mid-field by definition (Horner-Devine et al., 2015), as mixing by the wind will mix the plume to a specified depth regardless of the initial condition (Fong and Geyer, 2001; Hetland, 2005). In the plume's far-field, particularly in the middle of the Louisiana continental shelf, details of the near-field plume should not contribute to eddy suppression.

Another design choice that deserves consideration is the z^* vertical coordinate coupled with the lack of bathymetry smoothing. We think this is unlikely to be an issue because the plume is surface trapped in summer and we see no evidence of spurious mixing or flow impedance associated with the interaction of the layers and the unsmoothed bathymetry. The idealized experiments with variable bathymetry in Part I also suggest that the vertical coordinate choice, at least on the shelf, is unlikely to
430 contribute to eddy suppression.

An additional difference arises from lateral boundary treatment: ROMS uses repeat-year forcing with climatological nudging (only near the boundaries) to a data-assimilative HYCOM configuration, whereas MPAS-O evolves freely without lateral boundaries. Previous work with the ROMS model (Marta-Almeida et al., 2013) showed that salinity skill near the M-A plume



is largely insensitive to the choice of data-assimilative parent model. This, coupled with the circulation on the inner shelf (inshore of 50 m depth) being modulated by wind forcing (Zhang et al., 2012a, 2014), suggests MPAS-O's suppression of shelf eddies is unlikely to result from its freely evolving configuration.

Despite these limitations, MPAS-O: USGS still qualitatively captures the seasonal evolution of the M-A plume. This was demonstrated by tagging the M-A rivers with passive dyes and conducting a freshwater analysis shown in Fig. 9 similar to (Zhang et al., 2012a), which also highlights the strength of using a single regionally refined global mesh. It allows us to study the fate and transport of M-A discharge into the open GoM and possibly the north Atlantic with more simulation time— an analysis not possible with the ROMS model due to its limited domain. The model also shows promise in its ability to represent submesoscale dynamics in the open ocean, but this clearly requires further investigation. However, simulations that use interannual forcing should be performed so that the model can be validated against observations.

In this paper, we identified key challenges in configuring MPAS-O to simulate submesoscale coastal dynamics using regional refinement. Partly based on the results shown here, two-way nesting ROMS within MPAS-O is being evaluated by the DOE as an alternative to seamlessly integrate coastal and global submesoscale dynamics. We recommend that developers of other unstructured global models employ an idealized model hierarchy with increasing complexity to systematically assess model strengths and limitations; such an approach can clarify whether effort is best invested in improving a single modeling system or developing the coupling infrastructure required for nesting. Overall, our results indicate that substantial development is still required before MPAS-O can produce high-fidelity simulations in coastal regions dominated by submesoscale baroclinic instabilities. However, the improved performance on the TXLA shelf during winter—when submesoscale eddies are naturally suppressed—suggests that MPAS-O may be better suited for coastal systems characterized by weaker submesoscale activity, such as the Mid-Atlantic Bight.

Code and data availability. The following can be found at <https://doi.org/10.5281/zenodo.17903087>, which is an archived Zenodo repository (Schlichting et al., 2026): the E3SM branch with the GoM regionally-refined mesh used to produce the MPAS-O simulations, the COAWST branch used to produce the ROMS simulations, the supplementary material, and the model output and code needed to reproduce the figures. All river streamflow data is freely available from USACE (<https://www.mvn.usace.army.mil/>) and USGS (<https://waterdata.usgs.gov/nwis>) and also archived in the Zenodo repository. The HYCOM output used to force the ROMS simulations is freely available at <https://www.hycom.org/data/glb0pt08/expt-19pt1>.

Author contributions. D.R.S., K.M.S., and M.R.P contributed to the conceptualization, data curation, formal analysis, investigation, methodology, software, validation, visualization, writing the original draft, review & editing. R.D.H. contributed to the conceptualization, funding acquisition, methodology, supervision, review & editing. K.E.H contributed to the methodology, writing the original draft, review & editing. D.E. contributed to the funding acquisition, review & editing.



Competing interests. The authors declare they have no competing interests.

Acknowledgements. All authors were supported by the Study for Exascale Advances in a High-Resolution Ocean Using ROMS Coupled
470 to E3SM project funded through the U.S. Department of Energy, Office of Science and Office of Advanced Scientific Computing Research
Scientific Discovery through Advanced Computing program. The authors acknowledge that ChatGPT was used to assist with code cleaning
in the Zenodo archive and for grammar editing of the main text. This research used computational resources from the Perlmutter machine of
the National Energy Research Scientific Computing Center (NERSC), a U.S. Department of Energy Office of Science User Facility located
at Lawrence Berkeley National Laboratory, under Contract No. DE-AC02-05CH11231. Additional simulations and mesh development used
475 resources provided by the Los Alamos National Laboratory Institutional Computing Program, which is supported by the U.S. Department of
Energy National Nuclear Security Administration under Contract No. 89233218CNA000001.



References

- Balwada, D., Xiao, Q., Smith, S., Abernathy, R., and Gray, A. R.: Vertical fluxes conditioned on vorticity and strain reveal submesoscale ventilation, *Journal of Physical Oceanography*, 51, 2883–2901, <https://doi.org/10.1175/JPO-D-21-0016.1>, 2021.
- 480 Barkan, R., McWilliams, J. C., Molemaker, M. J., Choi, J., Srinivasan, K., Shchepetkin, A. F., and Bracco, A.: Submesoscale dynamics in the northern Gulf of Mexico. Part II: Temperature–salinity relations and cross-shelf transport processes, *Journal of Physical Oceanography*, 47, 2347–2360, <https://doi.org/10.1175/JPO-D-17-0040.1>, 2017a.
- Barkan, R., McWilliams, J. C., Shchepetkin, A. F., Molemaker, M. J., Renault, L., Bracco, A., and Choi, J.: Submesoscale Dynamics in the Northern Gulf of Mexico. Part I: Regional and Seasonal Characterization and the Role of River Outflow, *Journal of Physical Oceanography*, 47, 2325–2346, <https://doi.org/10.1175/jpo-d-17-0035.1>, 2017b.
- 485 Bracco, A., Liu, G., and Sun, D.: Mesoscale-submesoscale interactions in the Gulf of Mexico: From oil dispersion to climate, *Chaos, Solitons & Fractals*, 119, 63–72, <https://doi.org/10.1016/j.chaos.2018.12.012>, 2019.
- Burchard, H. and Rennau, H.: Comparative quantification of physically and numerically induced mixing in ocean models, *Ocean Modelling*, 20, 293–311, <https://doi.org/10.1016/j.ocemod.2007.10.003>, 2008.
- 490 Callies, J., Ferrari, R., Klymak, J. M., and Gula, J.: Seasonality in submesoscale turbulence, *Nature communications*, 6, 6862, <https://doi.org/10.1038/ncomms7862>, 2015.
- Danilov, S., Sidorenko, D., Wang, Q., and Jung, T.: The finite-volume sea ice–ocean model (fesom2), *Geoscientific Model Development*, 10, 765–789, <https://doi.org/10.5194/gmd-10-765-2017>, 2017.
- DiMarco, S. F. and Reid, R. O.: Characterization of the principal tidal current constituents on the Texas-Louisiana shelf, *Journal of Geophysical Research: Oceans*, 103, 3093–3109, <https://doi.org/10.1029/97jc03289>, 1998.
- 495 DiMarco, S. F., Howard, M. K., and Reid, R. O.: Seasonal variation of wind-driven diurnal current cycling on the Texas-Louisiana Continental Shelf, *Geophysical Research Letters*, 27, 1017–1020, <https://doi.org/10.1029/1999GL010491>, 2000.
- Engwirda, D.: JIGSAW-GEO (1.0): Locally orthogonal staggered unstructured grid generation for general circulation modelling on the sphere, *Geoscientific Model Development*, 10, 2117–2140, <https://doi.org/10.5194/gmd-10-2117-2017>, 2017.
- 500 Fong, D. A. and Geyer, W. R.: Response of a river plume during an upwelling favorable wind event, *Journal of Geophysical Research: Oceans*, 106, 1067–1084, <https://doi.org/10.1029/2000JC900134>, 2001.
- Fox-Kemper, B., Danabasoglu, G., Ferrari, R., Griffies, S., Hallberg, R., Holland, M., Maltrud, M., Peacock, S., and Samuels, B.: Parameterization of mixed layer eddies. III: Implementation and impact in global ocean climate simulations, *Ocean Modelling*, 39, 61–78, <https://doi.org/10.1016/j.ocemod.2010.09.002>, 2011.
- 505 Gent, P. R. and McWilliams, J. C.: Isopycnal mixing in ocean circulation models, *Journal of Physical Oceanography*, 20, 150–155, 1990.
- Golaz, J.-C., Lin, W., Zheng, X., Xie, S., Roberts, A., Roedel, L. P. V., Thornton, P. E., Barthel, A., Bradley, A., Wolfe, J. D., et al.: The Energy Exascale Earth System Model version 3. Part II: Overview of the coupled system, *ESS Open Archive eprints*, 446, essoar-175097464, 2025.
- Große, F., Fennel, K., and Laurent, A.: Quantifying the relative importance of riverine and open-ocean nitrogen sources for hypoxia formation in the northern Gulf of Mexico, *Journal of Geophysical Research: Oceans*, 124, 5451–5467, <https://doi.org/10.1029/2019JC015230>, 2019.
- 510 Hetland, R. and Hsu, T.: Freshwater and sediment dispersal in large river plumes, *Biogeochemical dynamics at large river-coastal interfaces: Linkages with global climate change*, pp. 55–85, <https://doi.org/10.1017/CBO9781139136853>, 2013.



- Hetland, R. D.: Relating river plume structure to vertical mixing, *Journal of Physical Oceanography*, 35, 1667–1688, <https://doi.org/10.1175/jpo2774.1>, 2005.
- 515 Hetland, R. D.: Suppression of baroclinic instabilities in buoyancy-driven flow over sloping bathymetry, *Journal of Physical Oceanography*, 47, 49–68, <https://doi.org/10.1175/jpo-d-15-0240.1>, 2017.
- Hetland, R. D. and DiMarco, S. F.: Skill assessment of a hydrodynamic model of circulation over the Texas–Louisiana continental shelf, *Ocean Modelling*, 43, 64–76, <https://doi.org/10.1016/j.ocemod.2011.11.009>, 2012.
- Higdon, R. L.: A two-level time-stepping method for layered ocean circulation models: further development and testing, *Journal of Computational Physics*, 206, 463–504, <https://doi.org/10.1016/j.jcp.2004.12.011>, 2005.
- 520 Hinson, K., Schlichting, D., Hetland, R. D., Engwirda, D., Smith, K. M., and Uyeda, K.: Towards High-Fidelity Simulations of Coastal Submesoscale Baroclinic Instabilities with MPAS-O Part I: Idealized Experiments, *Geoscientific Model Development*, 2026.
- Hoch, K. E., Petersen, M. R., Brus, S. R., Engwirda, D., Roberts, A. F., Rosa, K. L., and Wolfram, P. J.: MPAS-Ocean simulation quality for variable-resolution North American coastal meshes, *Journal of Advances in Modeling Earth Systems*, 12, e2019MS001848, <https://doi.org/10.1029/2019MS001848>, 2020.
- 525 Horner-Devine, A. R., Hetland, R. D., and MacDonald, D. G.: Mixing and transport in coastal river plumes, *Annual Review of Fluid Mechanics*, 47, 569–594, <https://doi.org/10.1146/annurev-fluid-010313-141408>, 2015.
- Jerlov, N. G.: Optical studies of ocean water, Rept. Swedish Deep-Sea Exped., 3, 1–59, 1951.
- Kobashi, D. and Hetland, R.: Reproducibility and variability of submesoscale frontal eddies on a broad, low-energy shelf of freshwater influence, *Ocean Dynamics*, 70, 1377–1395, <https://doi.org/10.1007/s10236-020-01401-4>, 2020.
- 530 Large, W. G., McWilliams, J. C., and Doney, S. C.: Oceanic vertical mixing: A review and a model with a nonlocal boundary layer parameterization, *Reviews of geophysics*, 32, 363–403, <https://doi.org/10.1029/94RG01872>, 1994.
- Li, Q., Reichl, B. G., Fox-Kemper, B., Adcroft, A. J., Belcher, S. E., Danabasoglu, G., Grant, A. L., Griffies, S. M., Hallberg, R., Hara, T., et al.: Comparing ocean surface boundary vertical mixing schemes including Langmuir turbulence, *Journal of Advances in Modeling Earth Systems*, 11, 3545–3592, <https://doi.org/10.1029/2019MS001810>, 2019.
- 535 Liu, G., Bracco, A., and Sitar, A.: Submesoscale mixing across the mixed layer in the Gulf of Mexico, *Frontiers in Marine Science*, 8, 615066, <https://doi.org/10.3389/fmars.2021.615066>, 2021.
- Luo, H., Bracco, A., Cardona, Y., and McWilliams, J. C.: Submesoscale circulation in the northern Gulf of Mexico: Surface processes and the impact of the freshwater river input, *Ocean Modelling*, 101, 68–82, <https://doi.org/10.1016/j.ocemod.2016.03.003>, 2016.
- 540 Marta-Almeida, M., Hetland, R. D., and Zhang, X.: Evaluation of model nesting performance on the Texas-Louisiana continental shelf, *Journal of Geophysical Research: Oceans*, 118, 2476–2491, <https://doi.org/10.1002/jgrc.20163>, 2013.
- Mathis, M., Logemann, K., Maerz, J., Lacroix, F., Hagemann, S., Chegini, F., Ramme, L., Ilyina, T., Korn, P., and Schrum, C.: Seamless integration of the coastal ocean in global marine carbon cycle modeling, *Journal of Advances in Modeling Earth Systems*, 14, e2021MS002789, <https://doi.org/10.1029/2021MS002789>, 2022.
- 545 McWilliams, J. C.: Submesoscale currents in the ocean, *Proceedings of the Royal Society A: Mathematical, Physical and Engineering Sciences*, 472, 20160117, <https://doi.org/10.1098/rspa.2016.0117>, 2016.
- McWilliams, J. C., Huckle, E., and Shchepetkin, A. F.: Buoyancy effects in a stratified Ekman layer, *Journal of Physical Oceanography*, 39, 2581–2599, <https://doi.org/10.1175/2009JPO4130.1>, 2009.
- Ntaganou, N., Chassignet, E. P., and Bozec, A.: Impact of horizontal model resolution on mixing and dispersion in the northeastern Gulf of Mexico, *Journal of Geophysical Research: Oceans*, 129, e2024JC021315, <https://doi.org/10.1029/2024JC021315>, 2024.
- 550



- Paulson, C. A. and Simpson, J. J.: Irradiance measurements in the upper ocean, *Journal of Physical Oceanography*, 7, 952–956, 1977.
- Petersen, M. R., Jacobsen, D. W., Ringler, T. D., Hecht, M. W., and Maltrud, M. E.: Evaluation of the arbitrary Lagrangian–Eulerian vertical coordinate method in the MPAS-Ocean model, *Ocean Modelling*, 86, 93–113, <https://doi.org/10.1016/j.ocemod.2014.12.004>, 2015.
- Petersen, M. R., Asay-Davis, X. S., Berres, A. S., Chen, Q., Feige, N., Hoffman, M. J., Jacobsen, D. W., Jones, P. W., Maltrud, M. E., Price, S. F., et al.: An evaluation of the ocean and sea ice climate of E3SM using MPAS and interannual CORE-II forcing, *Journal of Advances in Modeling Earth Systems*, 11, 1438–1458, <https://doi.org/10.1029/2018MS001373>, 2019.
- 555 Qu, L., Thomas, L. N., and Hetland, R. D.: Near-inertial-wave critical layers over sloping bathymetry, *Journal of Physical Oceanography*, 51, 1737–1756, <https://doi.org/10.1175/jpo-d-20-0221.1>, 2021.
- Qu, L., Thomas, L. N., Wienkers, A. F., Hetland, R. D., Kobashi, D., Taylor, J. R., Hsu, F. H. W., MacKinnon, J. A., Shearman, R. K., and Nash, J. D.: Rapid vertical exchange at fronts in the Northern Gulf of Mexico, *Nature communications*, 13, 1–11, <https://doi.org/10.1038/s41467-022-33251-7>, 2022.
- 560 Redi, M. H.: Oceanic isopycnal mixing by coordinate rotation, *Journal of Physical Oceanography*, 12, 1154–1158, [https://doi.org/10.1175/1520-0485\(1982\)012<1154:OIMBCR>2.0.CO;2](https://doi.org/10.1175/1520-0485(1982)012<1154:OIMBCR>2.0.CO;2), 1982.
- Ringler, T., Petersen, M., Higdon, R. L., Jacobsen, D., Jones, P. W., and Maltrud, M.: A multi-resolution approach to global ocean modeling, *Ocean Modelling*, 69, 211–232, <https://doi.org/10.1016/j.ocemod.2013.04.010>, 2013.
- 565 Ringler, T. D., Thuburn, J., Klemp, J. B., and Skamarock, W. C.: A unified approach to energy conservation and potential vorticity dynamics for arbitrarily-structured C-grids, *Journal of Computational Physics*, 229, 3065–3090, <https://doi.org/doi.org/10.1029/2019MS001954>, 2010.
- Schlichting, D., Qu, L., Kobashi, D., and Hetland, R.: Quantification of physical and numerical mixing in a coastal ocean model using salinity variance budgets, *Journal of Advances in Modeling Earth Systems*, 15, e2022MS003380, <https://doi.org/10.1029/2022MS003380>, 2023.
- 570 Schlichting, D., Hetland, R. D., and Jones, C. S.: Numerical mixing suppresses submesoscale baroclinic instabilities over sloping bathymetry, *Journal of Advances in Modeling Earth Systems*, <https://doi.org/10.1029/2024MS004321>, 2024.
- Schlichting, D., Smith, K., Petersen, M., Hetland, R., Hinson, K., and Engwirda, D.: Towards high-fidelity simulations of Coastal Submesoscale Baroclinic Instabilities with MPAS-O Part II: Data and Code, Dataset, <https://doi.org/10.5281/zenodo.17903087>, 2026.
- 575 Shchepetkin, A. F. and McWilliams, J. C.: Quasi-monotone advection schemes based on explicit locally adaptive dissipation, *Monthly weather review*, 126, 1541–1580, [https://doi.org/10.1175/1520-0493\(1998\)126<1541:QMASBO>2.0.CO;2](https://doi.org/10.1175/1520-0493(1998)126<1541:QMASBO>2.0.CO;2), 1998.
- Shchepetkin, A. F. and McWilliams, J. C.: The Regional Oceanic Modeling System (ROMS): A split-explicit, free-surface, topography-following-coordinate oceanic model, *Ocean modelling*, 9, 347–404, <https://doi.org/10.1016/j.ocemod.2004.08.002>, 2005.
- Shchepetkin, A. F. and McWilliams, J. C.: Computational kernel algorithms for fine-scale, multiprocess, longtime oceanic simulations, in: *Handbook of numerical analysis*, vol. 14, pp. 121–183, Elsevier, 2009.
- 580 Shcherbina, A. Y., D’Asaro, E. A., Lee, C. M., Klymak, J. M., Molemaker, M. J., and McWilliams, J. C.: Statistics of vertical vorticity, divergence, and strain in a developed submesoscale turbulence field, *Geophysical Research Letters*, 40, 4706–4711, <https://doi.org/10.1002/grl.50919>, 2013.
- Skamarock, W. C. and Gassmann, A.: Conservative transport schemes for spherical geodesic grids: High-order flux operators for ODE-based time integration, *Monthly Weather Review*, 139, 2962–2975, <https://doi.org/10.1175/MWR-D-10-05056.1>, 2011.
- 585 Smolarkiewicz, P. K. and Margolin, L. G.: MPDATA: A finite-difference solver for geophysical flows, *Journal of Computational Physics*, 140, 459–480, <https://doi.org/10.1006/jcph.1998.5901>, 1998.



- Sorourian, S., Huang, H., Xu, K., Justic, D., and D'Sa, E. J.: A modeling study of water and sediment flux partitioning through the major passes of Mississippi Birdfoot Delta and their plume structures, *Geomorphology*, 401, 108–109, <https://doi.org/10.1016/j.geomorph.2022.108109>, 2022.
- Stefan, H. G. and Preud'homme, E. B.: Stream temperature estimation from air temperature I, *Journal of the American Water Resources Association*, 29, 27–45, <https://doi.org/10.1111/j.1752-1688.1993.tb01502.x>, 1993.
- Stewart, K., Kim, W., Urakawa, S., Hogg, A., Yeager, S., Tsujino, H., Nakano, H., Kiss, A., and Danabasoglu, G.: JRA55-do-based repeat year forcing datasets for driving ocean–sea-ice models, *Ocean Modelling*, 147, 101–157, <https://doi.org/10.1016/j.ocemod.2019.101557>, 2020.
- Suzuki, T., Yamazaki, D., Tsujino, H., Komuro, Y., Nakano, H., and Urakawa, S.: A dataset of continental river discharge based on JRA-55 for use in a global ocean circulation model, *Journal of Oceanography*, 74, 421–429, <https://doi.org/10.1007/s10872-017-0458-5>, 2018.
- Taylor, J. R. and Thompson, A. F.: Submesoscale dynamics in the upper ocean, *Annual Review of Fluid Mechanics*, 55, 103–127, <https://doi.org/10.1146/annurev-fluid-031422-095147>, 2023.
- Thyng, K. M. and Hetland, R. D.: Seasonal and interannual cross-shelf transport over the Texas and Louisiana continental shelf, *Continental Shelf Research*, 160, 23–35, <https://doi.org/10.1016/j.csr.2018.03.006>, 2018.
- Turner, A. K., Lipscomb, W. H., Hunke, E. C., Jeffery, N., Engwirda, D., Ringler, T. D., Wolfe, J. D., et al.: MPAS-Seaice (v1. 0.0): sea-ice dynamics on unstructured Voronoi meshes, *Geoscientific Model Development*, 15, 3721–3751, <https://doi.org/10.5194/gmd-15-3721-2022>, 2022.
- Van Roekel, L., Adcroft, A. J., Danabasoglu, G., Griffies, S. M., Kauffman, B., Large, W., Levy, M., Reichl, B. G., Ringler, T., and Schmidt, M.: The KPP boundary layer scheme for the ocean: Revisiting its formulation and benchmarking one-dimensional simulations relative to LES, *Journal of Advances in Modeling Earth Systems*, 10, 2647–2685, <https://doi.org/10.1029/2018MS001336>, 2018.
- Warner, J. C., Sherwood, C. R., Arango, H. G., and Signell, R. P.: Performance of four turbulence closure models implemented using a generic length scale method, *Ocean Modelling*, 8, 81–113, <https://doi.org/10.1016/j.ocemod.2003.12.003>, 2005.
- Wiseman, W. J., Rabalais, N., Turner, R., Dinnel, S., and MacNaughton, A.: Seasonal and interannual variability within the Louisiana coastal current: stratification and hypoxia, *Journal of Marine Systems*, 12, 237–248, [https://doi.org/10.1016/S0924-7963\(96\)00100-5](https://doi.org/10.1016/S0924-7963(96)00100-5), 1997.
- Zhang, W. and Hetland, R. D.: A study of baroclinic instability induced convergence near the bottom using water age simulations, *Journal of Geophysical Research: Oceans*, 123, 1962–1977, <https://doi.org/10.1002/2017JC013561>, 2018.
- Zhang, X., Hetland, R. D., Marta-Almeida, M., and DiMarco, S. F.: A numerical investigation of the Mississippi and Atchafalaya freshwater transport, filling and flushing times on the Texas-Louisiana Shelf, *Journal of Geophysical Research: Oceans*, 117, <https://doi.org/10.1029/2012jc008108>, 2012a.
- Zhang, X., Marta-Almeida, M., and Hetland, R. D.: A high-resolution pre-operational forecast model of circulation on the Texas-Louisiana continental shelf and slope, *Journal of Operational Oceanography*, 5, 19–34, <https://doi.org/10.1080/1755876X.2012.11020129>, 2012b.
- Zhang, Y. J., Fernandez-Montblanc, T., Pringle, W., Yu, H.-C., Cui, L., and Moghimi, S.: Global seamless tidal simulation using a 3D unstructured-grid model (SCHISM v5. 10.0), *Geoscientific Model Development*, 16, 2565–2581, <https://doi.org/10.5194/gmd-16-2565-2023>, 2023.
- Zhang, Z., Hetland, R., and Zhang, X.: Wind-modulated buoyancy circulation over the Texas-Louisiana shelf, *Journal of Geophysical Research: Oceans*, 119, 5705–5723, <https://doi.org/10.1002/2013JC009763>, 2014.